JGR Oceans

RESEARCH ARTICLE

10.1029/2023JC020658

On the Mechanisms Driving Latent Heat Flux Variations in the Northwest Tropical Atlantic

Pablo Fernández[1], Sabrina Speich[1], Hugo Bellenger[1], Diego Lange Vega[2], Johannes Karstensen[3], Dongxiao Zhang[4], and Cesar Barbedo Rocha[5]

[1]Department of Geosciences, Laboratoire de Météorologie Dynamique, École Normale Supérieure, Paris, France, [2]University of Hohenheim, Institute of Physics and Meteorology, Stuttgart, Germany, [3]GEOMAR Helmholtz Centre for Ocean Research, Kiel, Germany, [4]CICOES/University of Washington and NOAA Pacific Marine Environmental Laboratory, Seattle, WA, USA, [5]Instituto Oceanográfico, Universidade de São Paulo, São Paulo, Brazil

Abstract The Northwest Tropical Atlantic (NWTA) is a region of complex surface ocean circulation. The most prominent feature is the North Brazil Current (NBC) and its retroflection at 8°N, which leads to the formation of numerous mesoscale eddies known as NBC rings. The NWTA also receives the outflow of the Amazon River, generating freshwater plumes that can extend up to 100,000 km^2. We show that these two processes influence the spatial variability of the region's surface latent heat flux (LHF). On the one hand, the presence of surface freshwater modifies the vertical stratification of the ocean, the mixed layer heat budget, and thus the air-sea heat exchanges. On the other hand, NBC rings create a highly heterogeneous mesoscale sea surface temperature (SST) field that directly influences the near-surface atmospheric circulation. These effects are illustrated by observations from the ElUcidating the RolE of Cloud-Circulation Coupling in ClimAte - Ocean Atmosphere (EUREC^{4}A-OA) and Atlantic Tradewind Ocean-Atmosphere Interaction Campaign (ATOMIC) experiments, satellite and reanalysis data. We decompose the LHF budget into several terms controlled by different atmospheric and oceanic processes to identify the mechanisms leading to LHF changes. We find LHF variations of up to 160 W m^2, of which 100 W m^2 are associated with wind speed changes and 40 W m^2 with SST variations. Surface currents or heat release associated with stratification changes remain as second-order contributions with LHF variations of less than 10 W m^2 each. This study highlights the importance of considering these three components to properly characterize LHF variability at different spatial scales, although it is limited by the scarcity of collocated observations.

Plain Language Summary The Northwest Tropical Atlantic (NWTA) is a region with a complex ocean circulation. It is dominated by the North Brazil Current (NBC), which parallel to the South American coast and changes its direction at 8°N. This leads to the formation of closed swirling circulations known as NBC rings. The NWTA also receives the outflow of the Amazon River. These two features affect the heat exchange between the ocean and the atmosphere associated with water evaporation (latent heat flux, LHF) as they modify sea surface temperature, salinity and the near-surface atmospheric circulation. Here, we use the observations collected from the ElUcidating the RolE of Cloud-Circulation Coupling in ClimAte - Ocean Atmosphere (EUREC^{4}A-OA) and Atlantic Tradewind Ocean-Atmosphere Interaction Campaign (ATOMIC) experiments, satellite data and combined observations with models to identify the key mechanisms leading to such LHF variations. More of 60% of them are associated to surface winds whilst sea surface temperature is behind a 25%. The Amazon outflow accounts for less than 10%. Although this study is limited by the paucity of oceanic, atmospheric and air-sea interface observations located at the same point in time and space, it highlights the importance of considering these three components to properly describe LHF variability.

Key Points:

- Latent heat flux (LHF) presents strong spatial variations in the northwest tropical Atlantic (NWTA), which has a complex ocean circulation
- Surface winds and sea surface temperature are the major drivers of LHF changes. The Amazon plume remains as a second-order contributor
- It is necessary to distinguish between spatial scales (mesoscale and below vs. large-scale) when assessing the ocean's influence on LHF

Correspondence to:

P. Fernández,
pablo.fernandez@lmd.ipsl.fr

Citation:

Fernández, P., Speich, S., Bellenger, H., Lange Vega, D., Karstensen, J., Zhang, D., & Rocha, C. B. (2024). On the mechanisms driving latent heat flux variations in the Northwest Tropical Atlantic. *Journal of Geophysical Research: Oceans*, *129*, e2023JC020658. https://doi.org/10.1029/2023JC020658

Received 11 NOV 2023
Accepted 1 APR 2024

Author Contributions:

Conceptualization: Cesar Barbedo Rocha
Investigation: Pablo Fernández, Hugo Bellenger
Project administration: Pablo Fernández
Resources: Hugo Bellenger, Diego Lange Vega, Johannes Karstensen, Dongxiao Zhang
Validation: Sabrina Speich
Writing – original draft: Pablo Fernández
Writing – review & editing: Pablo Fernández

1. Introduction

The Northwest Tropical Atlantic (NWTA, see Table A3 for a complete list of acronyms) near the estuary of the Amazon River is a region of complex surface ocean dynamics (Figure 1a, the black box delineating the NWTA) at the transition between equatorial and subtropical waters. The most prominent feature is the North Brazil Current (NBC), which flows northward parallel to the South American coast before retroflecting at about 8°N to form the North Equatorial Countercurrent. The NBC current system is closely associated with two major oceanic processes: the Amazon freshwater discharge (Reverdin et al., 2021) and the regular spawning of NBC rings (Johns et al., 1990; Richardson et al., 1994).

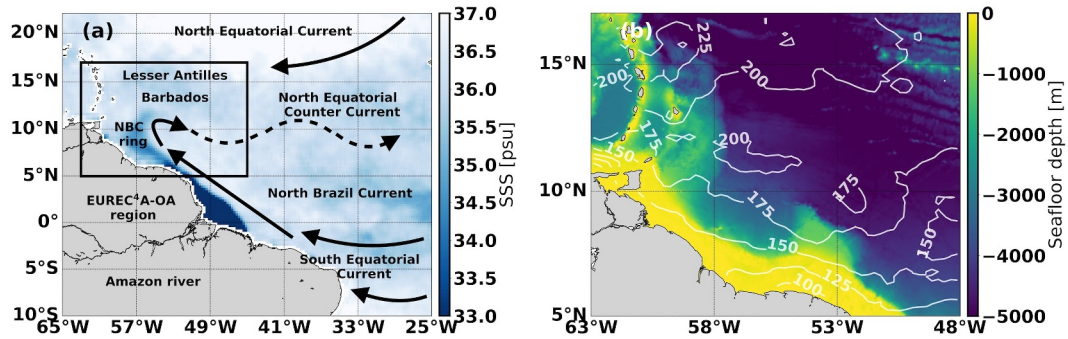

Figure 1. (a) Major dynamic features of the western equatorial Atlantic (arrows) superimposed on the SSS field averaged between seventeenth and 19 February 2020. The SSS field comes from the 4.0 version SMAP-SSS level 3, 8-day running mean gridded product (Boutin et al., 2021). The black box delineates what is referred to in the main text as the NWTA, the region where all the observations used in this article were measured. (b) Zoom in on the NWTA, the contours represent the mean February 2008-2018 LHF from SeaFlux (Roberts et al., 2020) and the shading shows the seafloor depth from the ETOPO2 product (Smith & Sandwell, 1997). Detailed information on all data sets in this figure can be found in Section 2.

With half of the total Atlantic discharge (Gévaudan et al., 2021) and one fifth of the global freshwater input from rivers to the ocean (Dai & Trenberth, 2002), the Amazon is the world's most important river system. The lateral extent of the Amazon River discharge, although minimal between January and March (Fournier et al., 2015), creates strong spatial heterogeneity in the sea surface salinity (SSS) field (Figure 1a), which also affects upper ocean temperatures. In fact, SSS can affect SST through its influence on the upper ocean stratification. When low salinity dominates the ocean stratification, the ocean layer in direct contact with the atmosphere, called the mixed layer (ML), becomes shallower. This situation is conducive to the formation of so-called barrier layers (BLs), which can support the development of a temperature inversion (Anderson et al., 1996; de Boyer Montégut et al., 2007; Foltz & McPhaden, 2009; Krishnamohan et al., 2019; Mahadevan et al., 2016; Mignot et al., 2012; Vialard & Delecluse, 1998). In the case of an established BL, heat and momentum inputs are often limited to the shallow ML, which responds faster to atmospheric forcing and cools (warms) more rapidly in winter (summer) as a consequence of the inhibition (enhancement) of the interaction with the deeper ocean (Miller, 1976; Sprintall & Tomczak, 1992). This leads to negative (positive) SST anomalies relative to their surroundings over the Amazon River plume and hence to reduced (increased) air-sea heat fluxes. However, the importance of this response is still debated, as observational studies suggest a strong impact (Foltz & McPhaden, 2009; Pailler et al., 1999) of BLs on SST, which models do not seem to reproduce (Balaguru et al., 2012; Breugem et al., 2008; Hernandez et al., 2016).

The shape and extent of the Amazon River plume is often modified by the local circulation induced by the NBC rings (Olivier et al., 2022; Reverdin et al., 2021) as it is shown in Figure 1a. They form at the NBC retroflection and move northwest toward the Lesser Antilles where they coalesce and dissipate due to their interaction with the complex topography represented in Figure 1b (Andrade-Canto & Beron-Vera, 2022; Fratantoni & Richardson, 2006; Jochumsen et al., 2010; Subirade et al., 2023). These eddies can modify the SST and SSS fields in the region in two different ways: by transporting the water trapped in their core during their formation (eddy trapping) and/or by stirring the surrounding waters, inducing the formation of cross-slope filaments that further cascade into smaller submesoscale structures (eddy stirring) (Olivier et al., 2022; Subirade et al., 2023). The NBC rings are characterized by a mean radius of 200 km (Fratantoni & Richardson, 2006), a vertical extension that varies between 200 and 300–1,000 m (Fratantoni & Glickson, 2002; Fratantoni & Richardson, 2006; Johns et al., 2003), azimuthal velocities between 0.1 and 0.17 m s^{-1} and a northwestward mean translation velocity between 8 and 15 km day^{-1} (Didden & Schott, 1993; Fratantoni & Richardson, 2006; Garraffo et al., 2003; Jochumsen et al., 2010; Johns et al., 2003). They play an essential role in the inter-hemispheric transport of mass, heat, salt, and biogeochemical properties of the ocean, and thus make an important contribution to the Atlantic Meridional Overturning Circulation (Johns et al., 2003). Most studies of NBC rings based on in situ observations have focused on their physical and biogeochemical properties (Olivier et al., 2022; Subirade et al., 2023). However, their impact on air-sea heat fluxes and in particular, on the latent heat flux (LHF) has not yet been assessed.

There is considerable evidence in the literature that mesoscale (O (10–200) km) SST gradients modify the lower atmosphere and hence air-sea heat fluxes. This fact has been assessed with satellite products (Bishop et al., 2017) and in situ observations (Acquistapace et al., 2022). There are two documented mechanisms driving such changes: the downward momentum mixing (DMM) (Hayes et al., 1989; Wallace et al., 1989) and the pressure adjustment (PA) (Lindzen & Nigam, 1987). In the DMM, the presence of warm SST anomalies destabilizes the marine atmospheric boundary layer (MABL) and enhances vertical motion. This favors the entrainment of drier air from the free troposphere into the MABL, thereby increasing the near-surface wind speed and the release of heat from the ocean in the form of latent heat flux (LHF) (Acquistapace et al., 2022). The PA mechanism, on the other hand, predicts that surface wind convergence (divergence) is generated over SST maxima (minima) as the warm (cold) SST patches generate surface pressure lows (highs). Reduced winds over SST extrema would lead to lower LHFs (Pasquero et al., 2021).

The effect of these two mechanisms has been documented from hourly to weekly time scales in several parts of the world ocean. Numerical investigations suggest that the relative importance of each of them depends on the background atmospheric stability (Foussard et al., 2019). PA tends to dominate in regions where surface winds are not effectively decoupled with the winds in higher levels. In turn, DMM dominates where the lower troposphere is stable and the SST effectively affects the magnitude of surface winds. Indeed, warm mesoscale eddies have been found to induce an increase in LHF with effects and surface winds, via DMM using satellite observations in the Southern Ocean (Frenger et al., 2013), in the Kuroshio extension (J. Ma et al., 2015) in the South China Sea (Liu et al., 2018), and in the Agulhas (O'Neill et al., 2005) and Malvinas (Villas Bôas et al., 2015) currents. Similar results have been obtained in the Gulf Stream region by means of a combination of operational weather analyses, satellite observations and an atmospheric general circulation model (Minobe et al., 2008). In addition, there is evidence that the submesoscale (O (1–10) km) SST gradients can also influence the surface wind response (Gaube et al., 2019; Meroni et al., 2018), significantly increasing LHF values when compared to coarser products (Shao et al., 2019). On the other hand, PA has been shown to affect clouds and precipitation in the cold wake of tropical cyclones (Z. Ma et al., 2020) through a cross-track secondary circulation (Pasquero et al., 2021). Here, LHF is reduced over the cold wake as a consequence of lower surface winds and cooler SSTs.

Using satellite data, Fernández et al. (2023) have evaluated the relative importance of DMM and PA in modifying the LHF in the northwestern tropical Atlantic. Here, LHF gradients exceeding 50 W m^{-2} are observed, a magnitude representing more than 40% of the climatology (Figure 1b). Fernández et al. (2023) find that the DMM largely dominates over the PA when the small-scale (features of less than 150 km) SST-near-surface-atmosphere interactions are considered. If the total increase in LHF per °C of SST is about 33% of the climatology, 28% is due solely to the changes in winds and specific humidity from the MABL thickening (dynamic contribution) and the remaining 5% is due to the fact that warmer air is able to hold more moisture (thermodynamic contribution).

The DMM thus provides the "top-down" physical mechanism by which the small-scale SST affects the near-surface atmosphere, a process known as the thermal feedback (TFB) (Renault et al., 2019). However, surface ocean currents also influence surface stress and wind in a "bottom-up" process known as the current feedback (CFB) (Bye, 1985; Chelton et al., 2001). A surface current anomaly with the same (opposite) direction as the surface wind speed creates a negative (positive) relative wind anomaly, thereby decreasing (increasing) LHF (Renault et al., 2016; Takatama & Schneider, 2017). Thus, statistically, the CFB does not have a systematic effect on the near-surface wind strength, as a current anomaly can induce a positive or negative wind anomaly depending on the relative orientation of the surface current to the surface wind. This mechanism was not investigated by Fernández et al. (2023).

The aim of this study is to quantify how all the processes described in the previous sections and linked with the ocean small-scale affect the LHF in the NWTA during winter. For this purpose, we use the in situ observations collected during the EUREC^{4}A-OA (ElUcidating the RolE of Cloud-Circulation Coupling in ClimAte - Ocean Atmosphere www.eurec4a.eu) and Atlantic Tradewind Ocean-Atmosphere Mesoscale Interaction Campaign (ATOMIC) field experiment (Stevens et al., 2021; Subirade et al., 2023). Aiming to better understand the interplay between clouds and shallow convection in the atmosphere, as well as small-scale air-sea interactions in the NWTA (and their role in climate), the EUREC^{4}A-OA and ATOMIC field experiments took place between the twelfth of January and the 23rd of February 2020. An unprecedented collection of high-resolution in situ observations were collected using state-of-the-art technology deployed from aircraft and ships and installed on autonomous vehicles (Karstensen et al., 2020; Quinn et al., 2021; Speich, 2021; Stevens et al., 2021). A wide

range of innovative and standard observing platforms were deployed, including Saildrones, ocean gliders, wave gliders, surface buoys, profiling floats, and 4 research vessels (RVs). The paper is organized as follows. The data sources are presented in Section 2. The different methods used to analyze the upper ocean, the air-sea interface and the vertical profiles of the atmosphere are described in Section 3, and 3.1 discussion of the main results is given in Section 4. A conclusion follows in Section 5.

2. Data

2.1. *In-Situ* Data

The EUREC^{4}A-OA/ATOMIC campaigns involved the participation of four RVs: RV *Atalante* from France (Speich, 2021), RV *Maria Sybilla Merian* hereafter referred to as *Merian* from Germany (Karstensen et al., 2020), RV *Meteor* from Germany (Mohr et al., 2020), and RV *Ronald Harmon Brown* hereafter referred to as *Ron Brown* from the United States (Quinn et al., 2021). These cruises provided numerous in situ measurements of the vertical structure of the ocean and atmosphere as well as the air-sea interface.

To study the vertical structure of the ocean in the NWTA, we use the vertical profiles of temperature, salinity and density from all sampling devices launched from the four RVs: CTDs; underway CTDs (uCTDs) (only from *Atalante*, *Merian* and *Meteor*), moving vessel profilers (MVP) (from *Atalante* and *Merian*), Argo profiling float measurements, a number of underwater electric gliders (Kraken, IFM03, IFM09, IFM12, SG579, SG620 and SG637) (Karstensen et al., 2020; Quinn et al., 2021; Speich, 2021; Stevens et al., 2021; Subirade et al., 2023). We remove the vertical profiles from which the salinity and/or temperature value closest to the surface are missing. We consider these values to be the SSS and SST and we need them in order to associate each profile to a water mass as detailed below. After this operation, we are left with 1,141 profiles in the NWTA with a vertical resolution of 0.5 m depth between 17 January 2020 and 16 February 2020. Special emphasis is placed on the 736 *Atalante* MVP vertical profiles sampled between the 2nd and the 5th of February 2020.

RV *Atalante* and RV *Merian* also provided many ship-based surface measurements. In particular, we use the air-sea interface measurements from the *Atalante* mast. Again, we focus on the mast data starting on 2 February 2020 and ending on 5 February 2020. They are provided at 1 s time resolution, although all data are averaged over 10 min intervals prior to all calculations to smooth out ship motion. The variables used include air pressure, relative humidity, air temperature and horizontal wind speed measured by the Vaisala WTX 520 weather station at 16 m for temperature and humidity and 17 m for wind speed. To compute the radiative forcing at the surface, we also use the net shortwave and longwave radiation fluxes provided by the Campbell CNR4 pyranometer and pyrgeometer installed on the mast. In addition, we exploit the SST-SSS values provided by the Seacat SBE21 thermosalinograph (TSG) at 5 m depth installed on the *Atalante*, and the X-band radar derived surface currents from the *Merian* between the 2nd and the 5th of February. We collocate both measurements with the *Atalante* meteorological mast to compute air-sea fluxes as described in Section A1 of the Appendix.

Between the second and the fifth of February 2020, 60 radiosondes (RS) were launched from the *Atalante* (Stephan et al., 2021). The RSs use water vapor mixing ratio (WVMR), pressure, relative humidity, air temperature, wind direction, wind speed, specific humidity, altitude, potential temperature. Each RS is associated with the nearest SST-SSS SBE21 TSG pair as described in Section A1 of the Appendix. In addition, the Atmospheric Raman Temperature and Humidity Sounder (ARTHUS, Lange et al. (2019)) and two Doppler lidars (DLs, Pearson et al. (2009)) from the University of Hohenheim were deployed and operated from the *Merian* between 25 January 2020 and 18 February 2020. In this study we focus only on the vertical profiles between the second and the fifth of February 2020 and use the low-resolution data version with averaged vertical profiles every 10 min, which allows us to filter out possible effects of ship motion. From ARTHUS we take the backscatter ratio (BR), air temperature and WVMR vertical profiles, which we then convert to specific humidity. From the DLs we take the horizontal and vertical wind speed vertical profiles. Note that while ARTHUS provides data from 225 to 3,025 m with 50 m spacing between levels, the vertical profiles from the DLs contain 56 vertical levels between 250 and 3,000 m with 50 m spacing. To resolve this mismatch, we perform a linear interpolation from the ARTHUS vertical resolution to the DLs vertical resolution (or a near-neighbor approximation if no data are available in the corresponding height level). Like before, we associate an SST-SSS pair from the *Merian* SBE38 TSG to each vertical profile.

Table 1
Information on the Devices Measuring Some of the Air-Sea Interface Variables Used in This Paper as Well as Their Installed Height in SD1063 and SD1064

Variable	SD1063 device	SD1064 device	Installed height
Air pressure	Vaisala Barometer 112,790	Vaisala Barometer 1,120,788	0.2
RH/Air temperature	Rotronic HC2-S3 AT/RH	Rotronic AT/RH (0,020,245,866)	2.3
Wind speed	Gill Anemometer (W182202)	Gill Anemometer (W181435)	5.2
Shortwave radiation	Delta-T Shaded Radiometer (A2047)	Delta-T Shaded Radiometer (A2045)	2.8
Longwave radiation	Eppley Radiometer (38873F3)	Eppley Radiometer (3277OF3)	0.8
Surface currents	Acoustic Doppler Current Profiler	Acoustic Doppler Current Profiler	−6

This study also benefits from the unprecedented view of the upper ocean at the air-sea interface provided by the three NASA-funded Saildrones (SD1026, SD1060 and SD1061) (Hall et al., 2022; L'Hégaret et al., 2022) and the two NOAA-funded Saildrones (SD1063 and SD1064) (Quinn et al., 2021; L'Hégaret et al., 2022) deployed during the EUREC^{4}A-OA/ATOMIC campaigns. These uncrewed surface vehicles sampled the upper ocean and the air-sea interface (Zhang et al., 2019) at very high temporal and spatial resolution (SD1026, SD1060, SD1061 and SD1063 sample at 1-min time resolution and SD1064 at 5-min rate). The three NASA Saildrones along with SD1063 monitored the ocean eddy corridor near the South American coast (see Figure 1 of Stevens et al. (2021) for specific locations) between January 17 and 2 March 2020, and January 13 and 5 March 2020, respectively. In turn, SD1064 passed over the eddy corridor and the open Atlantic Ocean (see Figure 1 of Stevens et al. (2021) for specific locations) during the period of January 13 to 11 April 2020.

We use SST and SSS measurements from all five Saildrones during the entire sampling period (from January to April). These two variables are collected by a SeaBirdE37-SMP-ODO microcat at 0.5 m depth in all cases. To compute LHF, we also consider surface pressure, near-surface horizontal wind components, near-surface relative humidity, which we then convert to specific humidity, air temperature, and surface currents (only available in SD1063 and SD1064). Details on the various instruments that measure these variables and their installation heights are given in Table 1.

2.2. Satellite and Reanalysis Data

We rely on daily satellite maps of SST, SSS and absolute dynamic topography (ADT) to provide a broad overview of the environmental conditions in which the in situ measurements take place.

The salinity maps are from the SMAP-SSS Level 3, 8-day running mean gridded product (Boutin et al., 2021). This product provides daily fields with a spatial resolution of 0.25°. The product is optimized for the Northwest Tropical Atlantic in February 2020 and is designed to provide the best possible representation of Amazon plume variability. The product, its uncertainties, and the comparison between TSG salinity and satellite SSS are detailed in Reverdin et al. (2021).

Daily SST maps are derived from the MUR-JPL data set. This satellite product provides high-resolution SST values distributed over a global $0.01° \times 0.01°$ grid. SST values from the version 4 Multiscale Ultrahigh Resolution (MUR) Level 4 analysis (Chin et al., 2017) are based on nighttime observations from several instruments, including the NASA Advanced Microwave Scanning Radiometer-EOS (AMSR-E), the JAXA Advanced Microwave Scanning Radiometer two on GCOM-W1, the Moderate Resolution Imaging Spectroradiometers (MODIS) on the NASA Aqua and Terra platforms, the US Navy WindSat microwave radiometer, the Advanced Very High Resolution Radiometer (AVHRR) on several NOAA satellites, and in situ SST observations from the NOAA iQuam project. Daily results are obtained using a multi-scale variational approach that combines all available observations. A comparison of this product with the SST observations collected during ATOMIC is presented in (Wick et al., 2023).

The satellite-based LHF is taken from the SeaFlux data set (Roberts et al., 2020). The SeaFlux version used in this paper is called SeaFluxV3 and uses a nonlinear neural network technique to estimate near-surface air properties from microwave radiances (Roberts et al., 2010). To compute surface turbulent fluxes from near-surface variables, SeaFlux uses a neural network version of the COARE3.0 algorithm (Fairall et al., 2003). This data set has a

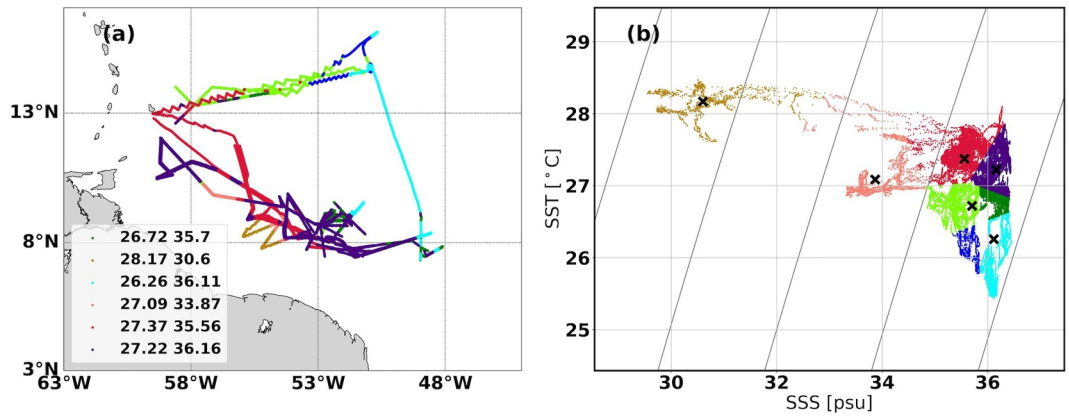

Figure 2. (a) Saildrone tracks color-coded by SST-SSS clusters. The values of the cluster centroids are shown in the legend, where the first value corresponds to the SST (in °C) and the second value represents the SSS (in psu). (b) T-S plot of all SST-SSS measurements taken by the Saildrones, color-coded with the water masses. The black crosses indicate the position of each cluster centroid in the diagram. Note that the green and cyan clusters are split in two according to an SSS threshold of 35.9 psu to account for the different origins of the water subtypes.

spatial resolution of nearly 25 km and a temporal resolution of 1 hr. Only daily averages of LHF are considered for the period 2008–2018.

To better understand the surface ocean circulation around the in situ measurements, we use the daily ADT maps at 0.25° resolution from the Global Ocean Gridded *L* 4 Sea Surface Heights And Derived Variables Reprocessed 1993 Ongoing product (CLS, 2018). It combines data from all available satellites for the period 1993 to present. With this ADT field, the TOEddies algorithm developed by Laxenaire et al. (2018) identifies eddies and their trajectories using the closed contours of the ADT as well as the maximum geostrophic velocity associated with the eddy. We also evaluate the seafloor depth map in the NWTA using the ETOPO2 data set (Smith & Sandwell, 1997) at a 2-min latitude/longitude spatial resolution.

To investigate the behavior of the marine atmospheric boundary layer height (MABLH) in regions where atmospheric in situ data are missing, we use the ERA5 reanalysis (Hersbach et al., 2020). Note that ERA5 does not include coupling with an ocean model, but it is forced at the lower boundary by the Hadley Center Sea Ice and Sea Surface Temperature (HadISST) data set as well as the Climate Change Initiative (ESA-CCI) until 2007 (Merchant et al., 2014) and the Operational Sea Surface Temperature and Ice Analysis (OSTIA) in the modern period (Donlon et al., 2007). ERA5 has a spatial resolution of 0.25° × 0.25° and a time resolution of 1 hr. We consider only the MABLH between second and fifth and between sixteenth and nineteenth of February 2020, which we collocate with the corresponding in situ observations as described in Section A1 of the Appendix.

3. Methodology

Prior to all calculations, we remove the diurnal cycle from several atmospheric and air-sea interface variables using a (multi-channel) singular spectrum analysis ((M-)SSA) (Groth et al., 2017). The imprint of diurnal warming on the near-surface circulation introduces an additional LHF variability source which masks the effects of some of the processes we want to assess here like the TFB and CFB effects. The reader is referred to Section A2 of the Appendix for a more detailed discussion on this point.

3.1. Water Mass Detection

We apply a *k-means* clustering method (Lloyd, 1982) to the SST-SSS fields from all five Saildrones to separate the different water masses sampled in the NWTA. We choose the Saildrone data fields to perform *k-means* because they sample the NWTA extensively (Figure 2a): from the relatively quiet open ocean to the active NBC eddy corridor region near the South American coast. In addition, their sampling period is the longest among all other sampling devices: from 13th January to 11 April 2020.

k-means requires a predetermined number of k clusters, followed by a series of evaluations to assess the performance of the previous clustering. The k mutually exclusive clusters are characterized by its centroid, and the SST-SSS observations are grouped according to their distance to this centroid in SST-SSS space, with the condition that the sum of the squared Euclidean distance within each cluster is minimized. After several tests, we set $k = 6$. This choice identifies six water masses with different oceanic vertical structures and allows us to link them to the physical mechanisms and situations in which they were formed.

3.2. Ocean Vertical Structure

We study the vertical stratification of the ocean using all the temperature, salinity, and density profiles collected by the 4 RVs. First, we apply a linear interpolation to all the vertical profiles to fill missing values and filter them with a five point moving average (2.5 m) to eliminate small-scale noise. Then, we compute the mixed layer depth (MLD) from the vertical density profiles as in Chen et al. (2022). To do so, we first estimate the gradient (first derivative) and curvature (second derivative) of the profiles using central differences. The derivatives along the profile edges are computed with one-sided differences. We then estimate the MLD as the depth with the maximum level of curvature, closest to the absolute maximum in potential density anomaly gradient, exceeding the surface density value by more than 0.03 kg m^{-3} and whose vertical gradient is greater than 0.0015 kg m^{-4}. Among other gradient and threshold methods, we find this MLD detection algorithm to be very sensitive to the effects of salinity variations on density in the NWTA.

$$\text{MLD} = \text{depth where} \begin{cases} \dfrac{\partial^2 \sigma_0}{\partial z^2} \text{ maximum closest to the } \dfrac{\partial \sigma_0}{\partial z} \text{ absolute maximum} \\ \sigma_0 > \sigma_{0,surf} + 0.03 \\ \dfrac{\partial \sigma_0}{\partial z} > 0.0015 \text{ kg m}^{-4} \end{cases} \tag{1}$$

where σ_0 is potential density anomaly with respect to a reference pressure of 0 dbar. In regions with strong salinity-driven stratification, such as river plumes, there may be some decoupling between haline and thermal stratification. Therefore, to characterize the relative importance of salinity in ocean stratification, we rely on the OSS_{MLD} indicator (Gévaudan et al., 2021; Maes & O'Kane, 2014):

$$OSS_{MLD} = \frac{\langle N_S^2 \rangle}{\langle N^2 \rangle}, \tag{2}$$

where angle brackets denote vertical integrals in the ocean profile down to the MLD, namely

$$\langle \bullet \rangle_{\text{MLD}} = \frac{1}{\text{MLD}} \int_{-MLD}^{0} \bullet \quad dz \tag{3}$$

N^2 represents the Brunt-Väisälä frequency and accounts for the total stratification of the ocean. It is expressed in terms of the density profile, the Earth's gravity (g), and the reference seawater density (ρ_0), which we set here to 1,026 g kg^{-3} as in Gévaudan et al. (2021):

$$N^2 = -\frac{g}{\rho_0} \frac{\partial \rho(T,S)}{\partial z} \tag{4}$$

The Brunt-Väisälä frequency can be decomposed as the sum of the stratification due to temperature (N_T^2) and the stratification due to salinity (N_S^2):

Table 2
Characteristic Values of the Different Seawater Coefficients Used in the Analysis of the Vertical Ocean Profiles

Constant	Value
ρ_0 [kg m^{-3}]	1,026
C_p [J kg^{-1} K^{-1}]	3,850
α [K^{-1}]	3.5 10^{-4}
β [kg g^{-1}]	0.78

Note. All of them are computed from temperature, salinity and pressure using the TEOS-10 Python module (McDougall et al., 2009).

$$N^2 = N_S^2 + N_T^2, \tag{5}$$

with

$$N_S^2 = \frac{g}{\rho_0}\frac{\partial\rho(T_0,S)}{\partial z} \quad \text{and} \quad N_T^2 = \frac{g}{\rho_0}\frac{\partial\rho(T,S_0)}{\partial z}. \tag{6}$$

T_0 and S_0 are constant representative temperature and salinity values equal to the average temperature and salinity values in the ML of each vertical profile. Like in Hernandez et al. (2016), we choose to calculate N_S^2 as the difference between N^2 and N_T^2. Therefore, OSS_{MLD} is the contribution of the salinity stratification N_S^2 to the total stratification N^2, both averaged in the ML, expressed as a percentage of N^2.

The decoupling of haline and thermal stratification leads to the formation of barrier layers (BLs) (Godfrey & Lindstrom, 1989; Lukas & Lindstrom, 1991). A quick inspection of all temperature, salinity, and density profiles shows that a shallow layer of constant salinity corresponding to the Amazon plume coexists with a thicker layer where temperature does not either decrease monotonically or remain almost constant. The former represents the actual ML computed from the density profiles while the latter corresponds to the existing ML before the inflow of the plume. As in de Boyer Montégut et al. (2004) and de Boyer Montégut et al. (2007), we define the lower boundary of that second layer (hereafter referred to as THERM) as the deepest level at which a temperature decrease of 0.2°C occurs with respect to the 10 m-depth temperature:

$$\text{THERM} = \text{depth where}[T = T_{10m} - 0.2\ ^\circ C] \tag{7}$$

We choose the 10 m depth temperature as the reference to avoid the effects of diurnal warming (we do not remove the diurnal cycle from the ocean vertical profiles as justified in Section A2 of the Appendix). Thus, the barrier layer thickness (BLT) is defined as the difference between THERM and MLD, where THERM is deeper than MLD (Sprintall & Tomczak, 1992). The presence of a BL limits the interaction between the ML and the ocean interior by inhibiting vertical water motion, thereby controlling the MLD heat content (OHC_{MLD}) per unit of area, which we estimate as:

$$OHC_{MLD} = \int_{MLD}^{0} \rho_0 C_p (T - T_{MLD}) \quad dz \tag{8}$$

where C_p is the specific heat capacity of seawater and T is water temperature. The presence of a surface fresh layer inhibits vertical mixing in the ocean as the layer's density is lower than that of the ocean below it. This situation is reversed if the surface fresher layer SST is lowered sufficiently by an amount ΔT that its effect on density ($\alpha\ \Delta T$) overcomes the stable density stratification provided by salinity ($-\beta\ \Delta S$). Where ΔS is the salinity difference between the fresh ML and the salinity just below it, β is the salinity contraction coefficient, and α is the thermal expansion coefficient. The values used for all constants are given in the Table 2. For a given cooling rate (Q), the temperature change achieved over an ocean layer of depth equal to the MLD in time Δt is:

$$\Delta T = \frac{Q\Delta t}{\rho_0 C_p MLD}. \tag{9}$$

Thus, the time taken to achieve the drop in temperature ΔT which overcomes ΔS reads (Mahadevan et al., 2016):

$$\Delta t = \frac{\rho_0\ C_p\ MLD}{Q}\frac{\beta\ \Delta S}{\alpha}. \tag{10}$$

Within the Amazon River plume, THERM is significantly deeper than the shallow MLD driven by salinity stratification. As shown in the next section, we often found warm temperature layers (and temperature inversions)

trapped between the MLD and THERM, whose excess stored heat is not always released to the atmosphere. An estimate of this heat is given by the following expression:

$$\text{Heat potentially released} = \frac{OHC_{THERM} - OHC_{MLD}}{\Delta t}. \quad (11)$$

Note that this heat release is not only necessarily in the form of LHF. An increase in SHF and surface outgoing long wave radiation (OLR) occurs at the same time. We will return to this point later.

So far, all calculations have been based on the vertical temperature, salinity, and potential density anomaly profiles. However, we also estimate the MLD from the SD1063 ADCP current shear profiles where no collocated vertical temperature, salinity and density profiles are available. To do this, we first perform a linear interpolation to the current profiles to fill missing values. Then, we compute the vertical shear profiles by applying a central difference scheme to the zonal and meridional ocean current vertical profiles. We expect the well-mixed ML to have a uniform current velocity. Thus, to identify the MLD, we select the absolute shear maximum, and if it exceeds a threshold of 5 10^{-4} s^{-1} (an empirical value chosen by the authors which works well for the data used as it avoids spurious MLD values related to small-scale peaks), it is considered to be an estimate of the MLD.

3.3. Air-Sea Interface

We compute LHF using the air-sea interface data from the RV *Atalante* meteorological mast, SD1063 and SD1064. This paper uses the COARE3.5 bulk algorithm to obtain LHF from SST, surface winds, surface humidity, and air temperature by applying the Monin-Obukhov Similarity Theory (MOST) (Edson et al., 2013; Fairall et al., 1996, 2003; Weller & Anderson, 1996). No rainfall or wave related corrections are considered, and fluxes are calculated from bulk SSTs. In addition, the cool skin correction to the SST is included in the LHF calculation when TSG SST data are involved.

To quantify the contribution of each LHF forcing variable to the flux variation, we follow the methodology used in Tanimoto et al. (2003); Chuda et al. (2008); Yang et al. (2016). After some mathematical steps (see Appendix) it can be shown that:

$$\Delta LHF = \rho_a L_e C_e \left[\underbrace{\Delta U\left(\overline{q_s} - \overline{q}\right)}_{\Delta \mathrm{LHF_U}} + \underbrace{\overline{U}\Delta q_s}_{\Delta \mathrm{LHF_{q_s}}} \underbrace{-\overline{U}\Delta q}_{\Delta \mathrm{LHF_q}} + \underbrace{\Delta U\left(\Delta q_s - \Delta q\right)}_{\Delta \mathrm{LHF_{U,\Delta q}}} \right] + \text{Residual}. \quad (12)$$

Here, overbars denote time averages and Δs represent the deviations from those averages. $\Delta \mathrm{LHF}_U$ represents the contribution of anomalous wind speed, $\Delta \mathrm{LHF}_{q_s}$ the contribution of anomalous saturation specific humidity (in other words, SST), and $\Delta \mathrm{LHF}_q$ the contribution of anomalous specific humidity. $\Delta \mathrm{LHF}_{U,\Delta q}$ is the effect on LHF due to the covariance between the anomalous wind speed and the specific humidity deficit, defined as the difference between saturation specific humidity and specific humidity. Finally, the residual ensures that the LHF budget closes. ρ_a, L_e, and C_e represent air density, latent heat of evaporation, and moisture exchange coefficient, respectively. They are obtained with COARE3.5 and averaged over time. The error associated with this averaging is included in the residual.

However, this decomposition does not distinguish between the large-scale and small-scale (oceanic mesoscale and below) contributions to ΔLHF, as in situ data contain the influence of all the different spatial scales. We know from the literature that this distinction is particularly important in the wind speed response, which is directly influenced by small-scale SST anomalies and surface currents (Renault et al., 2019).

To isolate the small-scale SST anomalies from the large-scale signal, we first identify the SST-SSS front as the mean SST value when the sampling device crosses the boundary between a low-salinity and a high-salinity water mass. We then estimate the small-scale SST anomalies (SST') as the difference between each SST value in the time series and this reference temperature. We then convert the small-scale SST anomalies to wind speed anomalies by multiplying by the coupling coefficient in the first row of Table 3 (α_{TFB}):

Table 3
Information on the Different Coupling Coefficients

Coefficient	Description	Value	Reference
α_{TFB}	SST and near-surface wind magnitude	0.44 m s^{-1} °C^{-1}	Fernández et al. (2023)
α_{CFB}	surface current vorticity and near-surface wind curl	0.3 (unitless)	Renault et al. (2019)

$$\Delta U_{TFB} = \alpha_{TFB}\, SST'. \tag{13}$$

The TFB contribution to the LHF is then computed by inserting ΔU_{TFB} into the terms ΔLHF_U and $\Delta LHF_{U,\Delta q}$ of Equation 12. To evaluate the impact of the CFB, we recall how the coupling with surface flows is performed in models (Renault et al., 2019). In a two-dimensional flow, the wind speed value of the equation is 12:

$$\vec{U} = \vec{U_a} - \vec{U_o}, \tag{14}$$

where $\vec{U_a}$ is the measured wind vector and $\vec{U_o}$ surface currents. In addition, surface currents feed back into $\vec{U}$ by an amount $\vec{\Delta U_{CFB}}$:

$$\vec{\Delta U_{CFB}} = \alpha_{CFB}\, \vec{U_o} \tag{15}$$

where α_{CFB} is the coupling coefficient between the surface current relative vorticity and the curl of surface winds. It is given in the second row of Table 3. Therefore, to estimate the effect of the CFB on the LHF, we first compute the terms ΔLHF_U and $\Delta LHF_{U,\Delta q}$ from Equation 12 using the wind velocity resulting from Equation 14. Then we calculate the same two terms using the winds from the difference between Equations 14 and 15. The difference between the two estimates of $\Delta LHF_U + \Delta LHF_{U,\Delta q}$ corresponds to CFB effect.

3.4. Atmospheric Vertical Structure

Data from ARTHUS and the DLs are used to study the vertical structure of the atmosphere. Following Acquistapace et al. (2022), we apply some preprocessing to remove noise and analyze the atmospheric response to the SSS-SST gradients. First, we remove values outside reasonable ranges. The selected valid ranges for the different variables are: from 0 to 20 g kg^{-1} for WVMR, from 270 to 310 K for air temperature, from −5 to 5 m s^{-1} for vertical wind speed, and from 0 to 20 m s^{-1} for horizontal wind speed. Since the air temperature decreases with height, its valid range is only between 200 and 3,000 m. Then we define the cloud base height (CBH) as 100 m (experimental value adopted by the authors) below the height where the largest vertical gradient in the BR occurs, as in Wang and Sassen (2001). The ARTHUS and DL values higher than the cloud base height are masked as they are known to be unreliable within the clouds (Lange et al., 2019).

We compute the marine atmospheric boundary layer height (MABLH) from the vertical LIDAR profiles after removing the diurnal cycle and applying the pre-processing described above. To this effect, we apply a rolling variance along each of the vertical WVMR profiles. We define the MABLH as the first maximum in the vertical WVMR variance profiles that exceeds a threshold of 0.2 g^2 kg^{-2} below 1,200 m height (experimental value adopted by the authors).

To increase the robustness of our results, we also include the MABLH computed from the different RSs launched from the *Atalante* (Stephan et al., 2021). As in Acquistapace et al. (2022), we assign an SST and SSS value from the *Merian* TSG to each RS. Then, we compute the virtual potential temperature gradient $\left(\frac{d\theta_v}{dz}\right)$ starting from a height level of 200 m. For a given height level, we calculate the mean and standard deviation of the distribution composed of all the vertical gradient values underneath. If the difference $\frac{d\theta_v}{dz}$ of the given height level and the mean of the distribution, as well as those from the three following levels exceed two times the standard deviation, then the MABLH is taken as the mean height between the above mentioned three vertical levels. This methodology has been found to disregard the high wind shear values close to the surface (likely due to the fast RS movements after

the deployment) while accounting for the presence of several θ_v inversions. The reader is referred to Section A3 of the Appendix for an intercomparison of different methods to compute MABLH from RS data.

Finally, we also compare the results with the collocated ERA5 MABLHs (more details on the collocation procedure in Section A1 of the Appendix). Following Renault et al. (2019) and as described in Fernández et al. (2023), the mesoscale MABLH anomalies are isolated from the large-scale signal using a spatial filter. The MABLH field is smoothed with an isotropic Gaussian spatial filter with a standard deviation of 4 grid points at 0.25°. Gaussian weights that are located at a distance greater than 3 standard deviations of the Gaussian (σ) are assumed to be zero. The Gaussian filter is thus applied to a $(6\sigma + 1) \times (6\sigma + 1)$, which is 25×25 points, and is roughly equivalent to $6° \times 6°$. The filter cutoff is about 250 km. Small scale anomalies of the MABLH are defined as MABLH' = MABLH - [MABLH], where [MABLH] is the smoothed field.

4. Results

4.1. A Very Heterogeneous Region: Water Mass Identification

The spatial distribution of the 6 surface water masses identified by the 5 Saildrones with *k-means* is shown in Figure 2a and their position in the T-S diagram in Figure 2b. North of Barbados, the domain is mostly dominated by the North Atlantic Subtropical Waters (NASWs) (similar to the NASWs in Olivier et al. (2022)) in light green (SSS <35.9 psu). The clustering analysis also detects waters with the same SST-SSS centroid at 9°N, 52.5°W, shown in dark green. These waters are saltier than the NASWs (SSS >35.9 psu). For simplicity, we include both waters in the same water mass, the green cluster waters (GCWs), since they all have SSTs around 26.72°C. In the transect from 13.5°N to 8°N, the farthest from the coast, we find the saltiest and coldest waters of the region (the cluster centroid values are 36.1 psu and 26.3°C, in blue). Again, in Figure 2 we distinguish between the waters with SSS less than 35.9 psu (dark blue), located north of 13°N, and those with SSS >35.9 psu (cyan), to highlight the different origins and locations. However, we will refer to these waters as cyan cluster waters (CCWs). They are also found in coastal upwelling systems, as shown later.

Closer to the coast, from 8°N to Barbados, we find four different water masses. In indigo we show the retroreflection waters (RWs), which are warm and salty (SST-SSS centroid of 27.22°C–36.16 psu). They are located south of 9°N and east of Trinidad and Tobago and are trapped within an anticyclonic NBC ring (A2 of Olivier et al. (2022)). North of the NBC retroflection we find the modified retroflection waters (MRWs) in purple. They are slightly warmer than the RWs (SST centroid of 27.37°C) and much fresher as a consequence of their interaction with the Amazon River outflow (SSS centroid of 35.56 psu).

Finally, we detect two low salinity clusters represented in gold and salmon colors Figure 2. The golden waters are the warmest and freshest (SST-SSS centroid of 28.17°C–30.6 psu) and are associated with the Amazon River plume. We refer to them hereafter as Amazon plume waters (APWs). They are found in the south of the NWTA, close to the continental shelf and mostly in the spring when the Amazon River discharge is at its highest during the period of study. The salmon cluster is also very fresh (33.87 psu as SSS centroid), but colder than the golden cluster (27.09°C as SST centroid). It results from the mixing of the colder and saltier RW and MRWs with the APWs, which are enhanced by the local ocean surface circulation induced by the NBC rings. In this paper, we call them modified Amazon plume waters (MAPWs).

The vertical ocean structure of the 6 water masses is shown in Figure 3. The GCWs and CCWs have uniform vertical profiles of temperature, salinity, and density down to the MLD, which is about 20 m (Figures 3a, 3b). The location of THERM is not significantly different from that of the MLD in the case of CCW whereas it is much deeper for GCW as a consequence of the presence of temperature inversions.

RWs and MRWs (Figures 3c and 3d respectively) show a well mixed salinity (between 35 and 36 psu) and density profile accompanied by a 45–55 m thick layer of almost constant temperature. Below this layer the temperature decreases. In both cases, the MLD lies below the THERM. In fact, over RWs we find the thickest MLDs of all the region (more than 100 m thick).

Salinity profiles of the APWs and MAPWs (Figures 3e and 3f, respectively), on the other hand, show a 10 m thick low-salinity layer associated with the Amazon plume, the base of which delimits the MLD. Temperature and density are also constant in this layer. Below the MLD, however, salinity and density decrease sharply while temperature remains constant until 20 m depth. It is the imprint of the ML prior to the advent of the plume. This

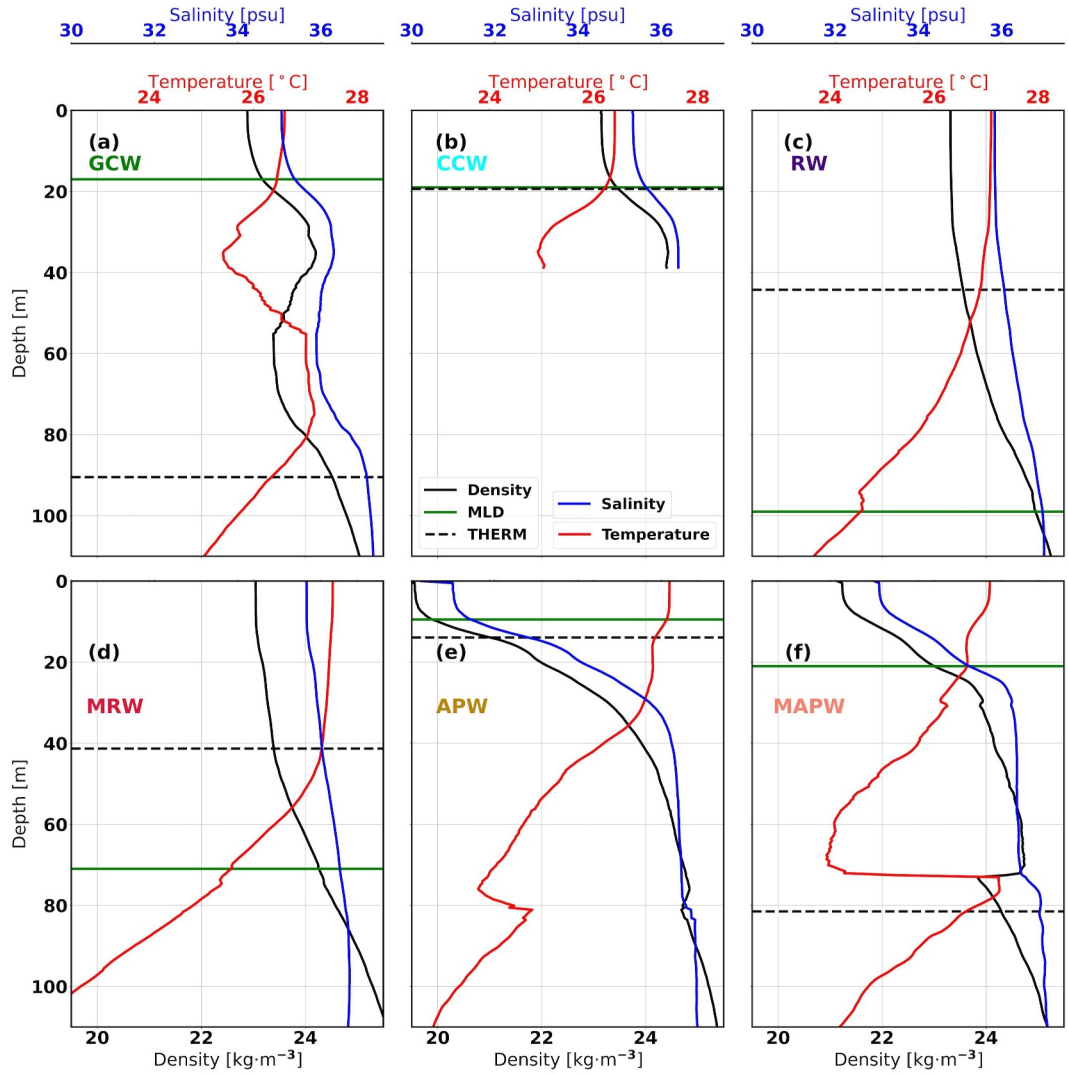

Figure 3. Mean vertical profiles of temperature (red), salinity (blue), and density (black) for (a) GCWs, (b) CCWs, (c) RWs, (d) MRWs, (e) APWs, and (f) MAPWs. In all figures, the solid green line marks the MLD and the dashed black line marks THERM. Data are collected from all ocean vertical profile sampling devices in Section 2.1 between January 17 and 16 February 2020.

situation creates a BL of about 10 m depth in APWs. Regarding MAPWs, THERM is located below the 2°C temperature inversion at 80 m depth. In both cases, there is also a slight salinity change at the same depth as the temperature inversion.

We also look at the evolution of LHF, 5.2 m wind speed (U_{5m}), 2.3 m specific humidity (q_{2m}), 2.3 m air temperature (T_{2m}), and SST over the different clusters as a function of SSS (Figure 4). Figure 4a shows reduced fluxes (around 150 W m^{-2}) for APWs and up to 34 psu and then a jump of 50 W m^{-2}. LHF is on average higher from 34.5 psu, but with a large spread. Furthermore, U_{5m} (Figure 4b) oscillates between 6 and 10 m s^{-1} with slightly lower values over the low salinity water masses. The SSS binning of q_{2m}, T_{2m} and SST is shown in Figures 4c–4e respectively. It shows larger values for the three variables over the low SSSs (19 g kg^{-1} for q_{2m}, 27.5°C for T_{2m}, and 28.2°C for SST) and smaller values over saltier waters (16.5 g kg^{-1}, 26.8°C, and 27.1°C). The trends in these three variables contribute to the increase of LHF at high salinity and are in agreement with the satellite climatologies of the NWTA, which show that higher (lower) specific humidity near (far) the coast and lower (higher) winds contribute to the decrease (increase) of LHF in this part of the region (open ocean) as shown in Fernández et al. (2023) and Figure 1b. However, Figure 4 does not allow us to separate the contributions of the different

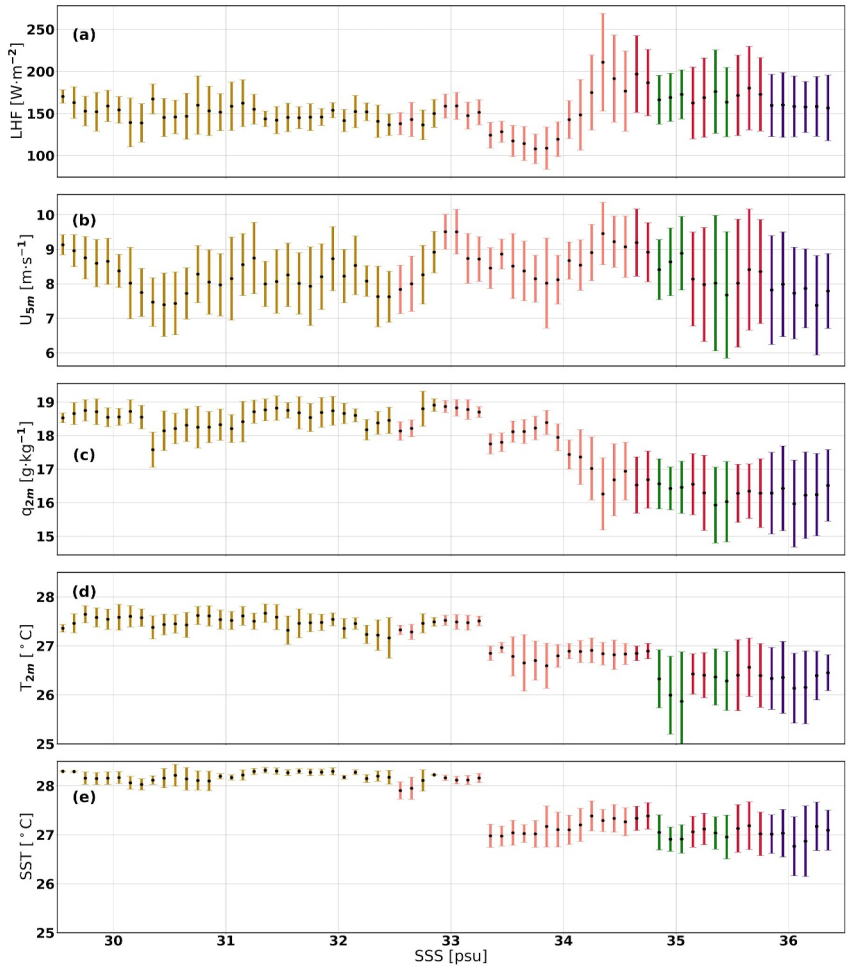

Figure 4. Binning in SSS 0.1 psu intervals of (a) LHF computed with COARE3.5, (b) U_{5m}, (c) q_{2m}, (d) T_{2m}, and (e) SST. The dots indicate the mean values in the interval and the error bars indicate the standard deviation. The error bars are color-coded with the water mass mode on each interval. Data are considered between 13th January and 11 April 2020.

forcing variables to the overall change in LHF. In the following sections, we aim to understand the different mechanisms leading to changes in the forcing variables and LHF, distinguishing between ocean, atmosphere, and air-sea interface processes, as well as between spatial scales. We do this with three study cases where the devices mentioned in Section 2.1 cross the freshwater Amazon plume.

4.2. Case 1: RVs *Atalante* and *Merian* Sample SSS-SST Front Caused by the Interaction Between the Amazon Plume and a Cold Coastal SST Patch

Between the second and the fifth of February 2020, RVs *Atalante* and *Merian* sampled a cold SST patch several times, as shown in Figure 5a. It developed near the coast of Suriname, probably as a consequence of an upwelling event (Acquistapace et al., 2022). The negative SST anomaly is associated with a cyclonic eddy in the ADT field, which we name C1 (Figure 5b). TOEddies also detects the presence of the NBC ring (A1) at 7°N and 51°W. The combined circulation of the two rings advects warm (Figure 5a) and fresh waters (Figure 5b) to the northwest, creating a 2°C-6 psu SST-SSS gradient. As a result, four different water masses were sampled: APW and MAPW toward the interior of the ocean and GCW and CCW closer to the continental shelf (Figure 5a).

Figure 6a contains the along track SST (red) and SSS (blue) values from the *Atalante* TSG. It shows that the SSS remained above 34 psu for the first 400 km and then dropped as the MAPWs and APWs were sampled. At the same time the SSTs crossed the 27°C threshold. We select four representative locations along the track (crosses in Figure 6a) and examine their vertical ocean structure. In Figure 6b we observe a 30 m thick well-mixed

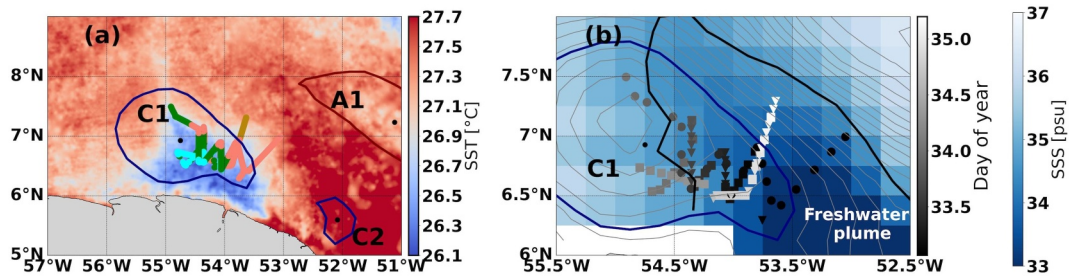

Figure 5. (a) Tracks of the various instruments sampling the SSS-SST front between the second and the fifth of February 2020, color-coded with the water masses they cross. The background shading indicates the mean MUR-JPL SST between the second and the fifth. (b) Zoom in on the tracks of the different instruments sampling the SSS-SST front, color-coded with the day of the year when each measurement was made. Squares represent the *Atalante* MVP, dots the ARTHUS/DLs vertical profiles, and inverted triangles the *Atalante* meteorological mast air-sea interface sites. The background shading indicates the mean SSS between second and 5 February 2020, and the black contour the mean 34.7 psu isoline chosen to delineate the Amazon plume. These last two features are obtained with the RS SMAP L3 SSS data set. The light gray contours represent the ADT isolines. In both panels, cyclonic (anticyclonic) eddies detected with TOEddies (Laxenaire et al., 2018) are represented by the closed blue (red) contours.

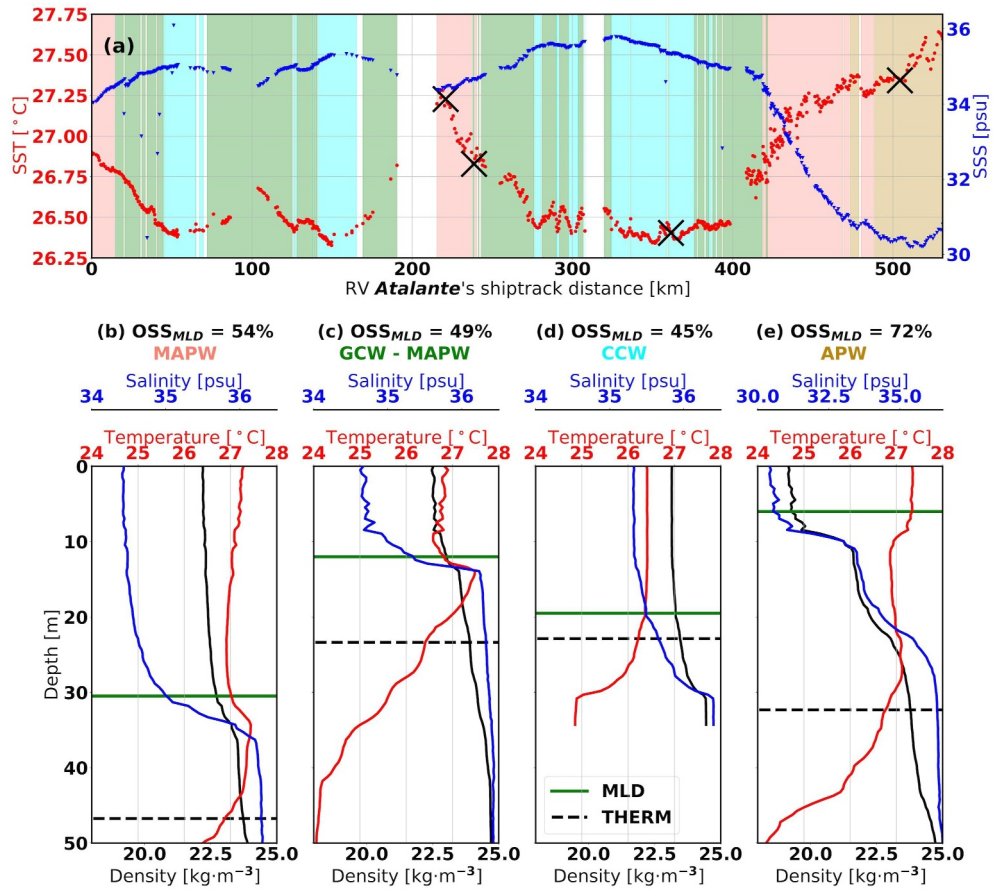

Figure 6. (a) RV *Atalante* TSG SST (red) and SSS (blue) time series between 2nd and 5th February 2020. The shading indicates the sampled water mass. The crosses mark the locations of the vertical profiles shown in panels (b), (c), (d), and (e), in the same order from left to right. Density is shown in black, temperature in red and salinity in blue. The MLD is shown as a solid green line and THERM as a dashed black line.

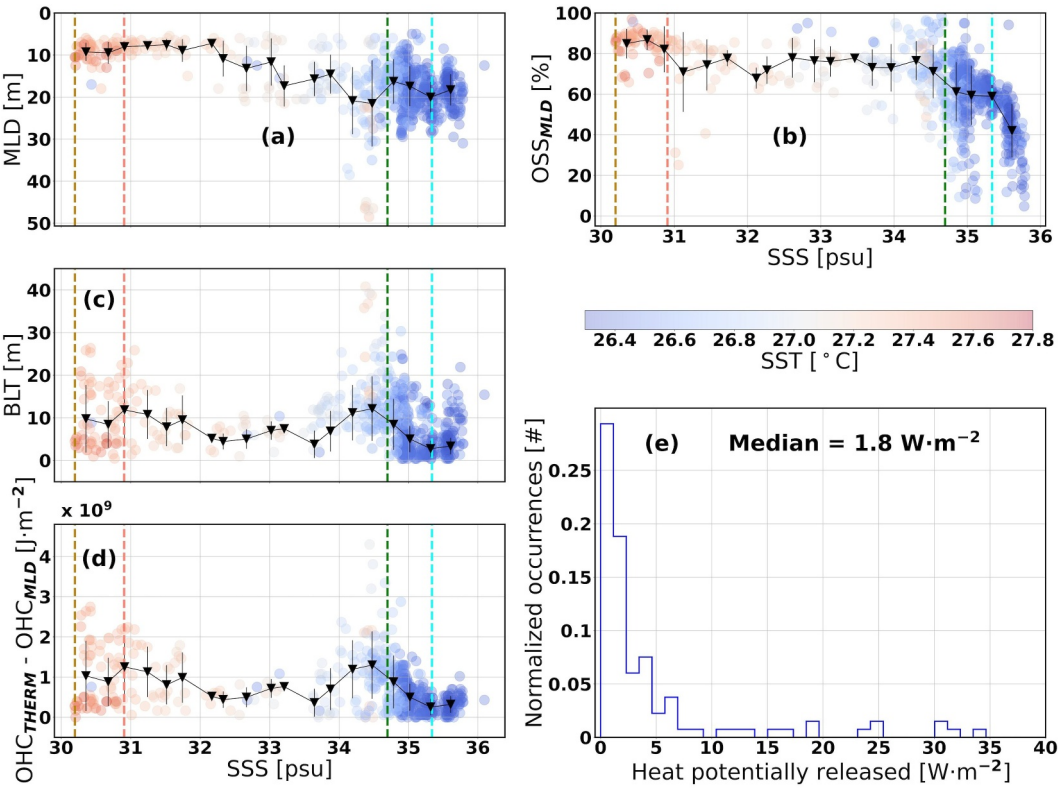

Figure 7. SSS binning of (a) mixed layer depth (MLD), (b) OSS_{MLD} index, (c) barrier layer thickness (BLT) computed as the difference between THERM and MLD, (d) ocean heat content per unit of area stored between THERM and the mixed layer depth. Colors indicate SST, and black lines, inverted triangles, and error bars indicate means and standard deviations within the 20 equal-width bins across the full salinity range. The colored dashed vertical lines indicate the freshest boundaries between clusters in the binning (color-coded with water mass as in Figure 2). (e) Shows the probability density function (PDF) of the heat potentially released to the atmosphere according to Equation 11 in waters between 34 and 35 psu.

temperature and salinity ML, with THERM 10 m above its base. As this profile belongs to the MAPWs, the SST is greater than 27°C and the OSS_{MLD} index is greater than 50%, meaning that salinity dominates over temperature in driving the stratification. However, as we approach the boundaries of the plume, but still in the MAPWs (in the transition between GCWs and MAPWs, Figure 6c), we find that salinity and temperature contribute equally to the stratification (OSS_{MLD} = 49%) and that the MLD is shallower than THERM (10 and 25 m, respectively). In between, we observe a warm subsurface layer with a temperature anomaly of 0.7°C warmer than the ML at its peak. In turn, the SST does not reach 27°C. On the other hand, the CCW profile (Figure 6d) shows a well mixed 20 m thick ML. Here MLD and THERM lie very close to each other and the BL is not able to develop as much as the other clusters. In addition, seawater temperature dominates over salinity in driving stratification (OSS_{MLD} of 45%). Finally, the APW profile (Figure 6e) shows a strong decoupling between thermal and haline stratification with a very fresh and warm ML of less than 10 m (OSS_{MLD} = 72%, salinity controlled stratification). THERM lies deeper than 30 m. Between the MLD and THERM we observe a layer of constant temperature with decreasing salinity (as shown in Figure 3f) which represents the existing ML before the inflow of the Amazon plume.

MLD estimates from all track locations derived from the *Atalante* MVP density profiles show the same tendency (Figure 7a, plotted as a function of RV *Atalante* TSG SSS, and color-coded with the TSG SST). Shallow 10 m ML are observed up to 32 psu, and their values increase with increasing SSS (decreasing SST), with MLDs as deep as 50 m. The OSS_{MLD} index shows the opposite tendency (Figure 7b). For low salinity values (APW and MAPW), salinity controls the vertical stratification of the ocean and the OSS_{MLD} index shows values as high as 80%–90%. Once the SSS exceeds the value of 34 psu, the OSS_{MLD} index starts to decrease and for the saltiest (coldest) part of the front, its values are less than 50%, meaning that the vertical stratification is controlled by sea temperature.

To quantify the decoupling between the influence of temperature and salinity on stratification, we compute the BLT as the difference between THERM and MLD when the former is deeper than the latter (Figure 7c). The BLTs are thicker within the APW (up to 30 m, in agreement with Figure 6e) and between SSS values of 34–35 psu (about 10–20 m), in agreement with Figures 6c and 6d respectively. The OHC difference between THERM and the MLD computed with Equation 8 shows the same pattern (Figure 7d), as it is proportional to the BLT by construction. However, it is interesting to focus on the increase of the OHC difference between 34 and 35 psu, which is accompanied by higher SSTs (light blue and some orange colors in the scatter dots). It corresponds to the heat stored in the subsurface warm layers found at the boundaries of the Amazon plume (Figure 6c, transition between MAPWs and GCWs). When the MLD salinity becomes large enough, the MLD waters become negatively buoyant and the atmospheric forcing (winds and radiative cooling of the boreal winter) is strong enough to overcome the plume-driven stratification, so that the subsurface warm layers are brought to the surface, increasing the SST and hence LHF. Therefore, we calculate the amount of heat potentially released using Equation 11 between 34 and 35 psu (Figure 7e) and obtain values between 0 and 35 W m^{-2}, being the median of the distribution 1.8 W m^{-2}. Note that this heat might not only be transferred to the atmosphere in the form of LHF, we also observe an increase in SHF and outgoing longwave radiation (OLR) as a result of the SST variations. However, they are small compared to the LHF change. Using COARE3.5 and the Stefan-Boltzmann law with the wind, humidity, temperature, and SST values shown in Figures 4, a 0.4°C SST increase as observed between Figures 6b and 6c leads to an LHF increase of 15.9 W m^{-2}, a SHF increase of 3.3 W m^{-2}, and an OLR increase of 2.5 W m^{-2}. However, for simplicity, we consider the histogram in Figure 7e to represent LHF only.

LHF is also influenced by the overlying atmospheric conditions and the atmospheric response to SST and surface currents. Previous research has already discussed the fast atmospheric response to this cold SST patch and its associated SSS gradient (Acquistapace et al., 2022), but failed to distinguish between spatial scales (mesoscale and below as opposed to large scales) and to evaluate its impact on LHF. Here we aim to answer the last two questions. To do so, we collocate the ARTHUS/DL vertical profiles measured by the RV *Merian* with the *Merian* TSG as described in Section A1 of the Appendix, and select the warmest 25% and the coldest 25%. A more detailed analysis of the horizontal wind speed and specific humidity vertical profiles follows in Section A4 of the Appendix. Figures 8a and 8b show that the warmest (coldest) profiles in salmon (cyan) are characterized by higher (lower) horizontal and vertical wind speeds at all levels. In turn, the warmest profiles down to 600 m have higher specific humidity than the coldest, in contrast to the situation above 600 m where the coldest profiles are more humid (Figure 8c). Whereas vertical velocity profiles seem to be in agreement with DMM, horizontal wind velocity vertical profiles do not. According to DMM we would expect higher surface wind speed over warm waters as observed, but also a larger wind shear owing to the decoupling between the MABL and the free troposphere. This last feature is not observed as horizontal wind speeds are lower in the coldest profiles for all the height levels. Thus, it seems that the changes in the horizontal wind speed profiles are more linked to temporal variations rather than spatial variations as discussed in Acquistapace et al. (2022). Indeed, the warmest profiles are all located at the end of the TSG SST time series. We come back to this point in the following paragraphs.

To check the MABLH thickness variations, Figure 8d contains the box plots of the coldest (left) and warmest (right) MABLH distributions using ARTHUS (red), the 60 *Atalante* RS (blue), and ERA5 (light green). In all three cases the MABLH is higher over the warm side with values ranging from 750 to 1,250 m. This result is consistent with the DMM mechanism and previous studies using bulk models of trade wind MABL dynamics (Neggers et al., 2006; Zheng, 2019), which show a decrease in MABLH over colder waters. Although the three estimates show the same trend, there is a large spread and mismatch between them because they were measured by different instruments at slightly different locations and using different methodologies. However, not all of the variations in MABL thickness, wind speed, and humidity are explained by the DMM mechanism. It is true that the MABLH' (in green) becomes positive over the warmest ERA5 grid points (between 0 and 150 m, as opposed to the -50–100 m range over the coldest grid points), as expected from the DMM. However, the smoothed MABLH field ([MABLH], in olive green) also increases from the cold to the warm side, implying that the large-scale atmospheric conditions are partly responsible for the regime change in the atmosphere.

To evaluate the impact of the above mechanisms on LHF, we apply Equation 12 to the RV *Atalante* mast air-sea interface data. We include the coupling with surface currents in the wind speed using Equation 14 and the collocated ocean surface velocity derived from the X-band radar on the RV *Merian*. A comparison between Equation 12 and a first-order numerical Taylor deconvolution can be found in Section A5 of the Appendix. Figure 9a shows the LHF deviations with respect to the along-track LHF mean between the second and the fifth of

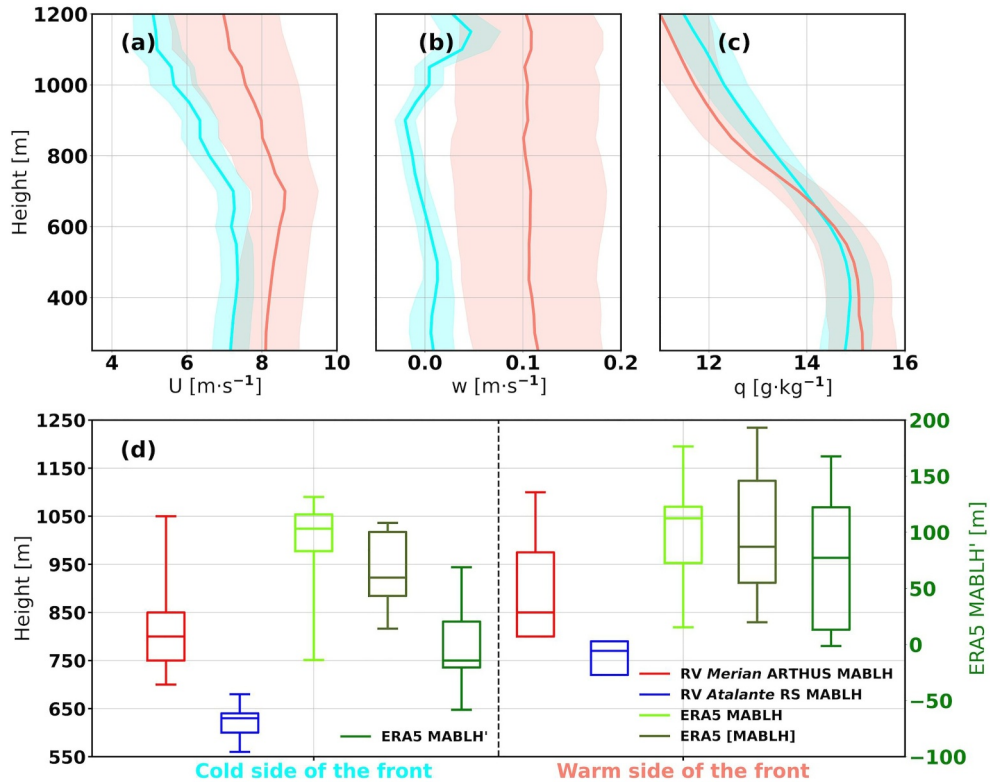

Figure 8. Averaged vertical profiles from the RV *Merian* ARTHUS/DL of (a) horizontal wind speed, (b) vertical wind speed, (c) specific humidity for the 25% lowest *Merian* TSG SSTs (cyan, color-coded with the mode cluster) and for the 25% highest *Merian* TSG SSTs (salmon, color coded with the mode cluster). Solid lines represent means and shading represents standard deviations. (d) Box plots of the MABLH calculated from the *Merian* ARTHUS (red), *Atalante* RS (blue), and collocated ERA5 data (lime green). The olive green box plots represent ERA5 [MABLH] and the green box plots represent MABLH'. The five left box plots correspond to the coldest SST values and the remaining five are computed over the warmest SST values. To maximize the number of observations per boxplot and since the SST values vary between data sets, here we choose the warm (cold) side of the front to be the warmest (coldest) most sampled water mass.

February. It shows a large LHF difference between both sides of the front of ∼160 W m^{-2}, close to the climatological LHF value (Figure 1b); the LHF is significantly lower over the cold SST patch. The near-surface wind influence (ΔLHF_U) shown in Figure 9b is the main controlling factor of the LHF variation ∼100 W m^{-2}. As shown in Figure 8a, APWs and MAPWs are associated with higher near-surface wind speeds and thus positive values of ΔLHF_U, which decrease as we move toward GCWs and CCWs.

The second most important term driving ΔLHF is ΔLHF_{q_s}, which represents LHF variations associated with SST changes and is shown in Figure 9c. APWs and MAPWs are associated with larger SSTs and thus positive ΔLHF_{q_s} values between 10 and 30 W m^{-2}. In turn, GCWs and CCWs are associated with negative ΔLHF_{q_s} values ∼ −10 to −20 W m^{-2}. In the boundaries of the Amazon plume, we observe a ΔLHF_{q_s} increase of ∼5 W m^{-2} on average (black triangles), associated with the release of heat from the subsurface warm layer, which coincides with the mean value of the probability density function shown in Figure 7e. Finally, the contributions of specific humidity (ΔLHF_q), the covariance between wind speed anomalies and specific humidity deficit anomalies ($\Delta LHF_{U,\Delta q}$) and the residual are second order contributions (Figures 9d–9f respectively). The first one shows values between −30 and 30 W m^{-2} over GCW and CCW with no clear tendency and the last two oscillate between 10 and −10 W m^{-2} over the whole SSS range.

Finally, we examine the total effect of wind speed on LHF ($\Delta LHF_U + \Delta LHF_{U,\Delta q}$), separating the effects of the TFB, the CFB, and the large-scale atmospheric circulation. Their mean values over each cluster, color-coded with the water mass, are shown in the first, second, third, and fourth bars of each quartet in Figure 10. Over the warm water masses (APW and MAPW), the near-surface wind speed increase associated with the DMM mechanisms

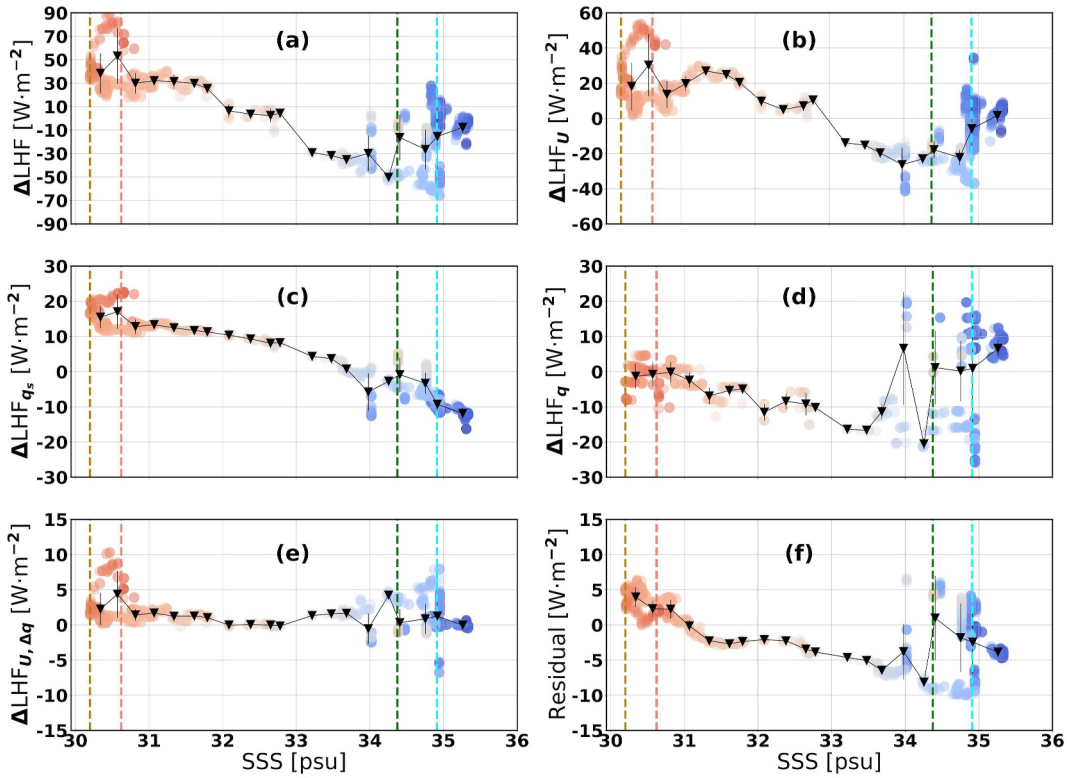

Figure 9. SSS binning of the various terms in Equation 12 (a) ΔLHF, (b) ΔLHF_U, (c) ΔLHF_{q_s}, (d) ΔLHF_q, (e) $\Delta LHF_{U,\Delta q}$, and (f) residual. As in Figure 7, the colors in the markers denote *Atalante* TSG SST values (same color scale), and the black lines and error bars denote means and standard deviations within 20 bins over the full salinity range. The vertical dashed lines represent the freshest salinity boundaries between the four clusters.

causes a positive TFB effect on LHF (4.5 and 2 W m^{-2}, respectively). Over the colder and saltier water masses (GCW and CCW), TFB has a negative effect on the LHF by reducing the near-surface winds. On the other hand, CFB always has a positive effect on LHF (except over APW where we lack collocated surface current data). This is due to the fact that trades flow toward the southwest while surface currents flow over most of the places toward the northeast (contours Figure 5b, see local circulation induced by C1). To sum up, TFB and CFB significantly contribute to total wind contribution to LHF ($\Delta LHF_U + \Delta LHF_{U,\Delta q}$) and can even drive the sign of it like in MAPWs.

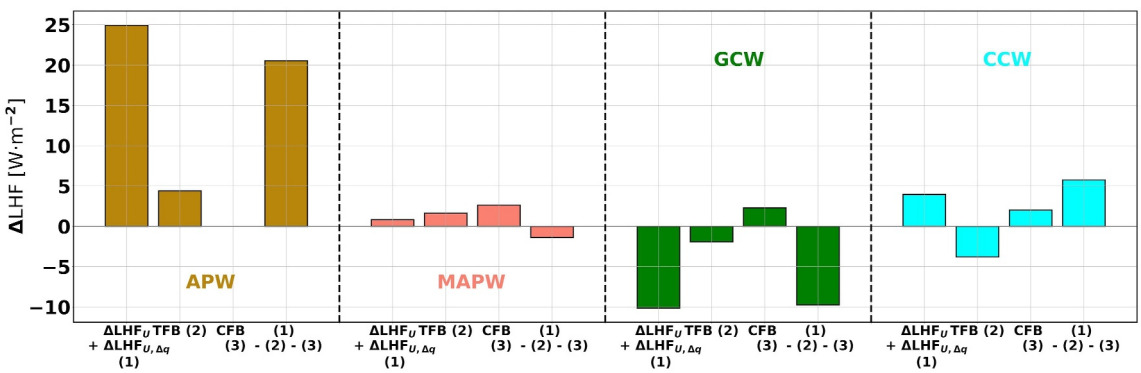

Figure 10. TFB and CFB evaluation in the four water masses. In each bar quartet, from left to right, the bars represent $\Delta LHF_U + \Delta LHF_{U,\Delta q}$, the LHF change as a consequence of the TFB, the LHF change associated with the CFB, and the difference between the first and the sum of the second and third. Same color code as in Figure 2.

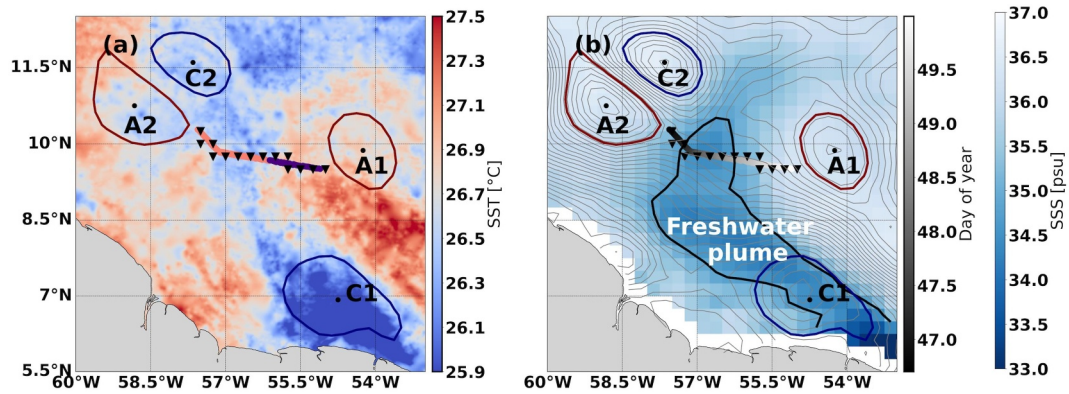

Figure 11. (a) Track of SD1063 sampling the SSS-SST front between sixteenth and 19 February 2020, color-coded with the water masses it crosses. The background shading indicates the mean MUR-JPL SST between the same dates. (b) Track of SD1063 color-coded with the time of each measurement. The gray contours correspond to the ADT isolines, and the thick black contour delimits the freshwater plume defined by the 34.7 psu isoline. The background shading indicates the mean RS SMAP L3 SSS between sixteenth and 19 February 2020. In both panels, cyclonic eddies are represented by thick blue contours and anticyclonic eddies by thick red contours, and the triangles represent the collocated ERA5 data. Mesoscale eddies are detected with TOEddies (Laxenaire et al., 2018).

4.3. Case 2: SD1063 Crossing a Weaker Amazon Plume Close to the NBC Retroflection

The NOAA-funded SD1063 crossed the northern edge of the Amazon plume between sixteenth and nineteenth in February 2020 (Figure 11). The local ocean surface circulation is driven by two different structures: the warm anticyclonic ring A1 and the anticyclonic-cyclonic eddy pair A2-C2. The clockwise rotation of the surface waters around A1 advects cool waters coming from the same coastal cold patch of Section 4.2 toward the northwest (Figure 11a), which mix with the low-salinity Amazon plume waters (Figure 11b). Thus, in this study case we work with two clusters: the cooler and fresher MAPWs in salmon and the warmer and saltier RWs in indigo (Figure 11a).

Figure 12 shows the binned distributions of different air-sea variables in both water masses. Note that, contrary to what happened in Section 4.2, the fresh side of the front is cooler than the warm side of the front, although the SST difference is not as large: on average 0.4°C as shown in Figure 12a (as opposed to 2°C). The specific humidity deficit, defined as the difference between the saturation specific humidity (q_s) and the specific humidity, also shows larger values over the RWs (~6 g kg^{-1}) than over the MAPWs (~4 g kg^{-1}), due to the SST changes via q_s and the background conditions that affect specific humidity as discussed later.

Figure 12c shows that surface wind speeds were on average higher over RWs (mean values between 9 and 10 m s^{-1}) than over MAPWs (mean values between 8 and 9 m s^{-1}). The surface winds also experienced a shift in direction, from northeast in RWs (~−115°) to east over MAPWs (~−100° to −90°), as shown in Figure 12d, although there is a lot of overlap between the two PDFs. This is the expected distribution for a region where the trades dominate the near-surface atmospheric circulation. On the other hand, the velocity of the surface currents, shown in Figure 12e, oscillates between 0.1 and 0.6 m s^{-1} in both cases, with average values slightly higher over the MAPWs due to the proximity of A2 and the associated compression of the ADT isolines (Figure 11b). These surface currents have mean directions of about −45° for RWs and −55° with respect to the north for MAPWs, as shown in Figure 12f. These directions are consistent with the ADT isolines of Figure 11b, from which we can deduce a southwest-northeast motion as a consequence of the combined effect of the clockwise rotation of A1 and the counterclockwise rotation of C2.

To get an insight into the vertical structure of the ocean in both water masses, we use the SD1063 ADCP data to compute the MLD from the shear maximum (MLD_{shear}), since no collocated vertical profiles of ocean temperature, salinity, and density are available. The results are shown in Figure 12g. Over MAPWs, the MLD is between 10 and 50 m depth, while RWs shows MLD_{shear} values between 40 and 70 m, as we expect the low salinity Amazon plume intrusion to determine stratification and reduce the thickness of the ML. The ERA5 collocated MABLH (black triangles in Figure 12) is shown as the solid line distribution in Figure 12h. It shows larger MABLH values over RWs (between 800 and 1,400 m) than over MAPWs (between 700 and 1,200 m). However, the MABLH'

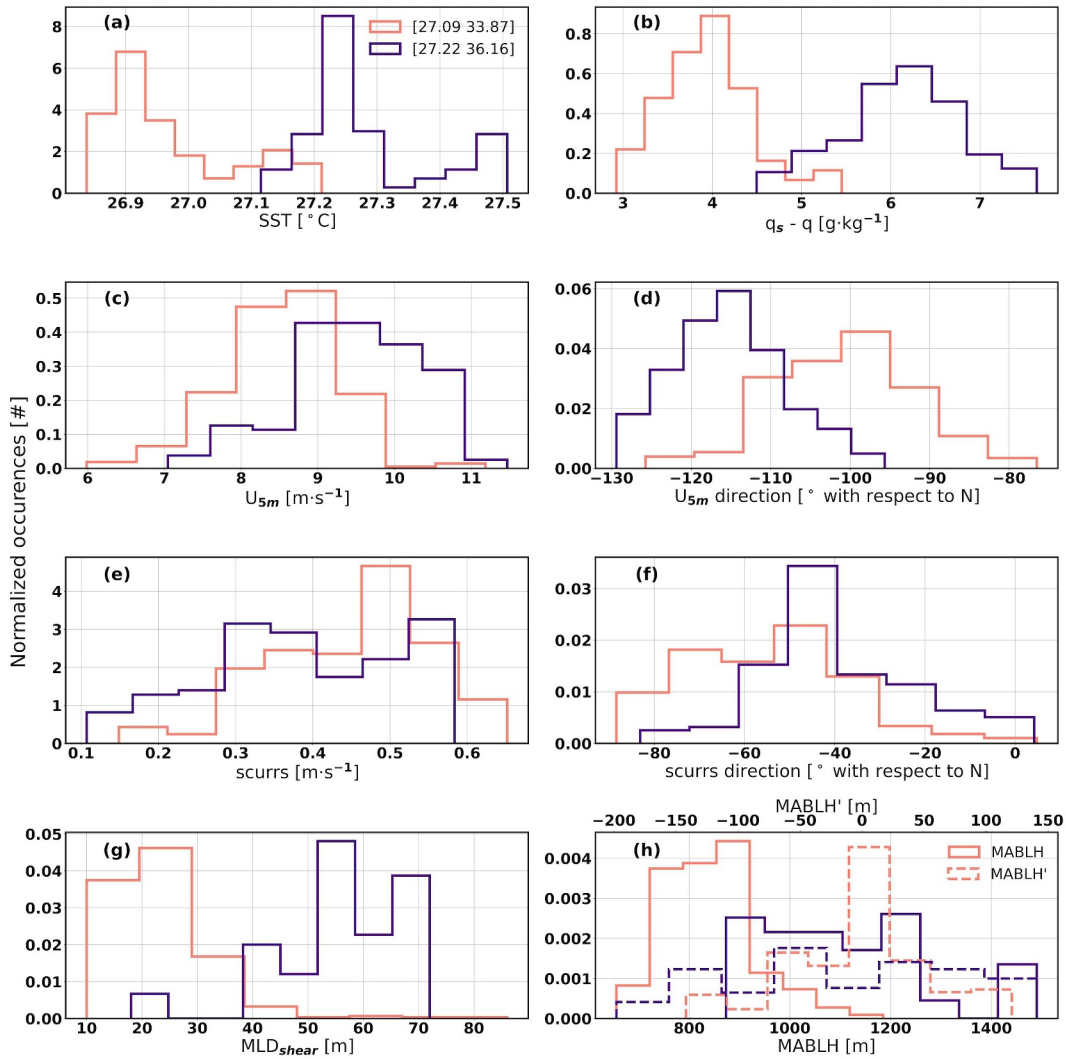

Figure 12. Histograms of the various Saildrone air-sea variables. (a) SST; (b) specific humidity deficit, defined as the difference between saturation specific humidity (computed as in Buck (1981)) and $q_{2.3m}$; (c) 5.2 m wind speed and (d) 5.2 m wind direction; (e) surface current norm and (f) surface current direction; (g) MLD computed from the shear maximum (MLD_{shear}); (h) collocated ERA5 MABLH (solid) and MABLH' (dashed). The probability density functions (PDFs) in all panels are color-coded with the cluster to which they belong. The [SST-SSS] centroids of each cluster are shown in the legend of (a). Data were collected between sixteenth and nineteenth of February 2020.

representing small-scale MABLH variations (dashed distributions) covers the same range of values for both water masses. Considering the ERA5 MABLH as a reliable data source (see Sections A1 and A4 of the Appendix for a detailed discussion), we conclude that the higher wind speed and lower specific humidity leading to an increase in the specific humidity deficit shown in Figures 12b and 12c may not be fully related to a near-surface response to mesoscale SST anomalies via the DMM mechanism, but mainly to a change in background conditions.

To compute the LHF and analyze its spatial variations, we use COARE3.5 and the decomposition in Equation 12. The results are shown in Figures 13a and 13b. LHF is on average 90 W m^{-2} higher over RWs than over MAPWs, mainly due to the large differences in specific humidity (green bars, ΔLHF_q, ∼60 W m^{-2} greater over RWs than over MAPWs) as a first order contributor and wind speed variations (blue bars, ΔLHF_U, ∼15 W m^{-2} greater over RWs than over MAPWs). The LHF variation directly driven by SST (red bars, ΔLHF_{q_s}, ∼10 W m^{-2} greater over RWs than over MAPWs) is the third most important contribution in both cases (red bars), while the covariance between wind speed and specific humidity gradient ($\Delta LHF_{U,\Delta q}$) and the residual, plotted in pink and orange, respectively, are the least important contributions.

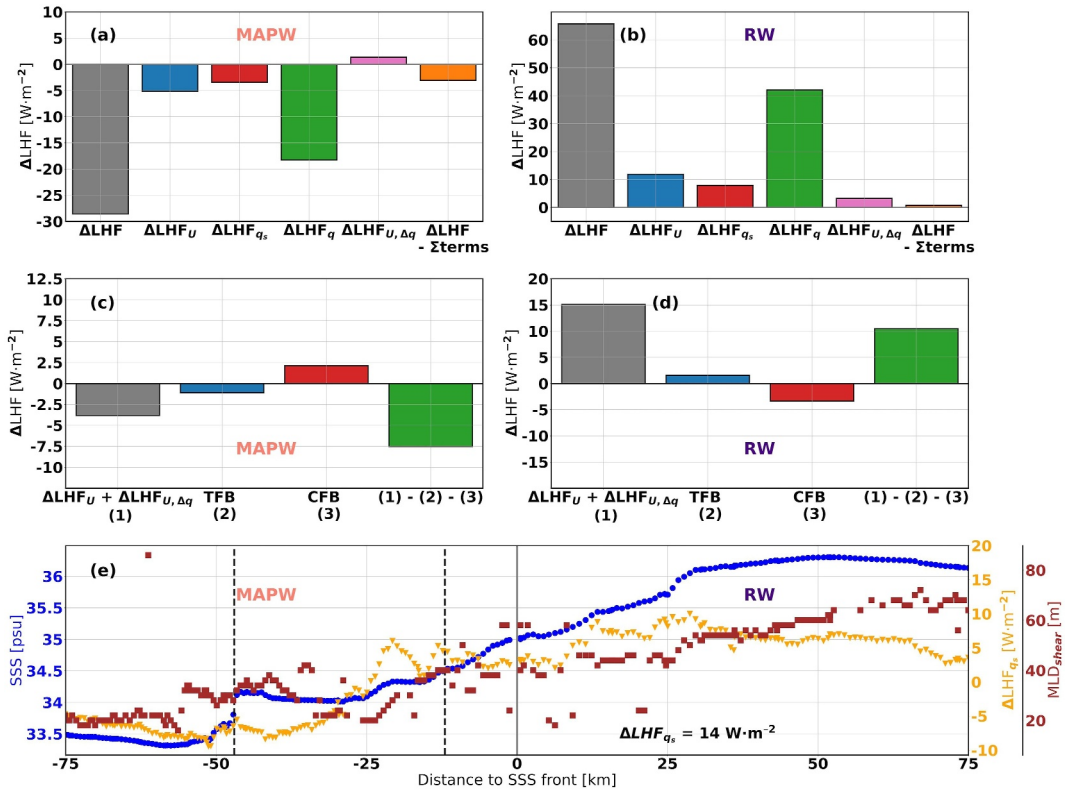

Figure 13. (a) and (b) show the LHF decomposition for the MAPWs and RWs, respectively. The bars in each plot represent from left to right: ΔLHF, ΔLHF_u, ΔLHF_{q_s}, ΔLHF_q, $\Delta\text{LHF}_{U,\Delta q}$, and residual. (c) and (d) depict from left to right the decomposition of the total wind speed contribution to the LHF change ($\Delta\text{LHF}_U + \Delta\text{LHF}_{U,\Delta q}$), the TFB contribution, the CFB contribution, and the background contribution. (e) Time series of SSS (blue), ΔLHF_{q_s} (yellow), and MLD_{shear} (brown) across the SSS front (defined as the location where the water mass changes). Data were acquired between 16th and 19th February 2020.

These results suggest that the spatial flux variations (i.e., the differences between the Gy bars in Figures 13a and 13b) are mainly driven by the atmosphere. In the case of the wind speed related LHF variations ($\Delta\text{LHF}_U + \Delta\text{LHF}_{U,\Delta q}$), we separate the influences of the background flow, the TFB and the CFB in Figures 13c and 13d. They show that $\Delta\text{LHF}_U + \Delta\text{LHF}_{U,\Delta q}$ is mainly driven by the background flow (green bar, ~ -7.5 W m^{-2} over MAPW vs. $\sim$10 W m^{-2} over RWs), with the CFB playing a secondary role in MAPWs and RWs(~ -2 and $\sim$2.5 W m^{-2} respectively). The TFB does not contribute significantly to $\Delta\text{LHF}_U + \Delta\text{LHF}_{U,\Delta q}$ with less than 1 W m^{-2} variation in both cases.

We also assess the effect of heat release from the subsurface warm layer with the time series of SSS and ΔLHF_{q_s}, plotted in blue and yellow in Figure 13e. They are displayed as a function of the distance to the SSS front defined between the last MAPW and the first RW measurements. The ΔLHF_{q_s} and SST are not uniform on both sides of the front, especially over MAPWs. At a distance between 50 and 10 km from the front in the MAPW domain, we find SSS values ranging from 34 psu to 35 psu (the boundaries of the Amazon plume, shown as vertical dashed lines) and a sharp increase in ΔLHF_{q_s} (of $\sim$14 W m^{-2}), which then remains constant for the rest of the track. This ΔLHF_{q_s} variation is of the same order of magnitude as the one shown in Figure 7e, occurs in the same salinity range as the secondary ΔLHF_{q_s} maximum in Figure 9c is analyzed over the same waters of Section 4.2 which have onlyn been advected northwestward. These facts suggest that the jump in ΔLHF_{q_s} could be related to heat release from the subsurface warm layer, although a more complete understanding of the vertical structure of the ocean and its evolution would be needed to verify this hypothesis. Finally, we also plot the alongshore MLD_{shear}. Consistent with Figure 12g, it is shallower over MAPWs and deepens with increasing SSS in RWs.

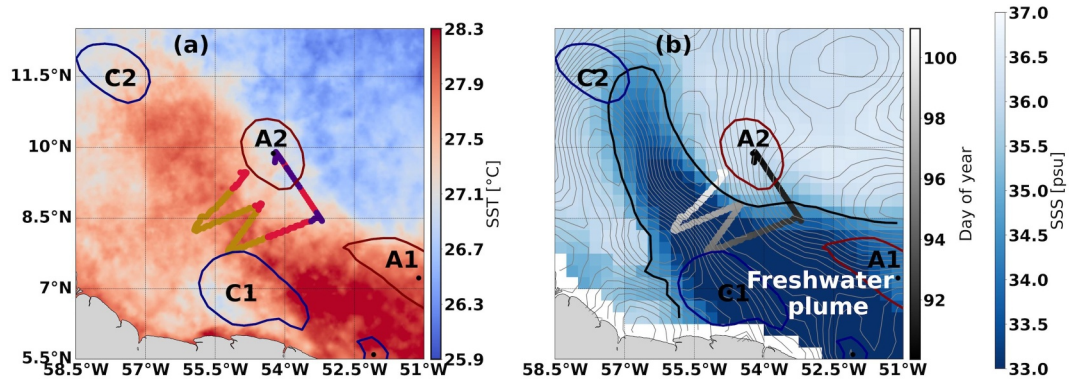

Figure 14. (a) Track of SD1064 sampling the freshwater plume front between 31st March and 11 April 2020, color-coded with the water masses it crosses. The background shading indicates the mean MUR-JPL SST between the same dates. (b) Track of SD1064 color-coded with the time of each measurement. The gray contours correspond to the ADT isolines, and the thick black contour delineates the freshwater plume defined by the 34.7 psu isoline. The background shading indicates the mean RS SMAP L3 SSS between 31st March and 11 April 2020. In both panels, cyclonic eddies are represented by thick blue contours and anticyclonic eddies by thick red contours. Mesoscale eddies are detected with TOEddies (Laxenaire et al., 2018).

4.4. Case 3: SD1064 Zigzagging Across a Strong Amazon River Plume in Boreal Spring

Between 31st March and 11th April, SD1064 zigzagged across a very warm and fresh water tongue as shown in Figures 14a and 14b. The freshwater plume detached from the Guiana Plateau at 6°N and was being steered northward by the induced circulation of the NBC ring A2 and the cyclonic C2 eddy (Figure 14) as well as by NBC retroflection. It then began to expand northeastward toward the open ocean. Between March 31 and April 3, SD1064 sampled RWs and MRWs (in indigo and crimson, respectively, in Figure 14a) and then entered and zigzagged across the plume, sampling APWs (in gold, the cluster with the lowest SSS centroid, 30.6 psu). This configuration gives an SST difference of less than 1°C between the inside and outside of the plume, but a very large SSS difference of more than 6 psu.

Based on the SD1064 TSG measurements, SSS values remained constant during the first three days of RW and MRW sampling (~36 psu) and then dropped to nearly 30 psu during the fifth of April (blue curve in Figure 15a). On April 6, SD1064 exited the plume and the SSS increased abruptly to 36 psu, then dropped back to 30–31 psu as SD1064 re-entered the plume. SST measurements show the opposite pattern, remaining below 28°C over RWs and MRWs and crossing the threshold during sampling of APWs. Note that the 28°C threshold is important because it provides moisture to the air column and favors tropical cyclone formation and intensification (Balaguru et al., 2012).

The total LHF anomaly time series, computed with respect to the mean LHF of the time period of this study case, is shown as a black line in Figure 15b, and its variability is a consequence of the combined effects of ΔLHF_U and ΔLHF_q (blue and red lines in Figure 15b, respectively). Between the 31st of March and the 2nd of April, SD1064 passed through a drier air mass (verified with the ERA5 specific humidity field, but not shown here), which increased ΔLHF_q and also Δ LHF, even though the wind speed anomalies and thus ΔLHF_U were negative during the same period. In fact, it is in the 2nd of April that ΔLHF reaches its lowest value, ~65 W m^{-2}. During the rest of the study period, ΔLHF variations were controlled by ΔLHF_U, which remained positive throughout most of the APW, in part due to the DMM mechanism. The fact that ΔLHF_U varies rapidly within hours and that ΔLHF_q shows less hourly variability reinforces the hypothesis that the specific moisture-associated flux changes originate from large-scale atmospheric variability.

Some of the second-order contributions to the LHF variations (ΔLHF_{q_s} in black, $\Delta LHF_{U,\Delta q}$ in blue, and the residual in red) are plotted in Figure 15c. Except for the first 3 days, $\Delta LHF_{U,\Delta q}$ and the residual are negligible for most of the period. In turn, the direct influence of the SST on the flux (ΔLHF_{q_s}) induces an LHF difference of ~45 W m^{-2} between the lowest point reached on the second of April over the MAPWs (~-25 W m^{-2}) and the highest point on the ninth of April (~20 W m^{-2}). Finally, the TFB and CFB time series are shown in Figure 15d. Except for the first three days of the time series, where there are significant negative TFB effects on the flux

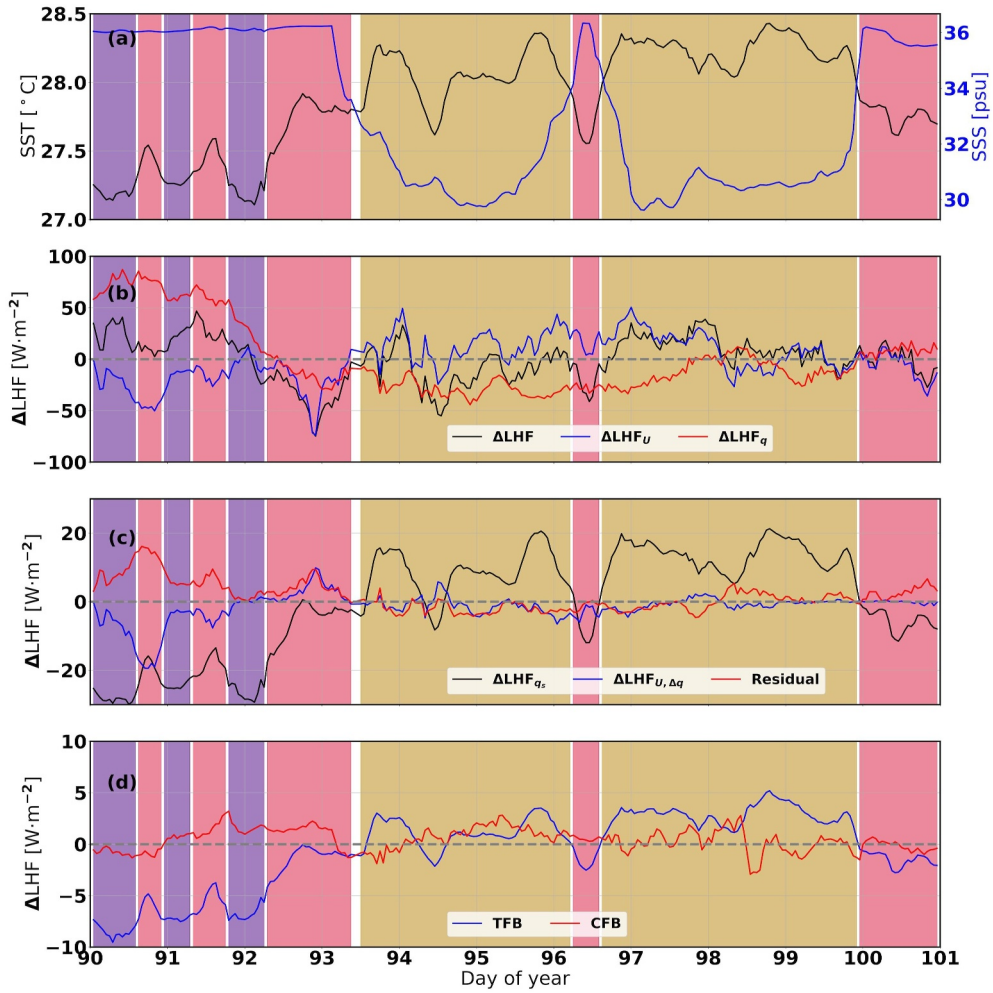

Figure 15. Time series along the SD1064 track of (a) TSG SST (black), SSS (blue); (b) ΔLHF (black), ΔLHF_U (blue) and ΔLHF_q (red); (c) ΔLHF_{q_s} (black), $\Delta LHF_{U,\Delta q}$ (blue) and residual (red); (d) TFB (blue) and CFB (red). The background color indicates the crossed water mass (see definition in Figure 2.

(between −10 and −5 W m^{-2}), in the rest of the time series the TFB and CFB are negligible and of the same order as $\Delta LHF_{U,\Delta q}$ and the residual. Note that we do not plot the collocated ERA5 MABLH values in this study case: they are noisy and do not allow us to draw any conclusions. This fact highlights the limitations of ERA5 to properly characterize MABLH dynamics and the importance of ocean-atmosphere coupling, especially at the ocean small scales.

5. Discussion and Conclusions

The EUREC^{4}A-OA/ATOMIC field experiment provides a large set of air-sea interface measurements and collocated ocean and atmosphere vertical profiles that allow us to investigate the influence of small-scale ocean dynamics on air-sea LHF variability in the NWTA between January and April 2020. To determine the influence of different small-scale ocean dynamics regimes, we divide the domain into different regions corresponding to different surface water masses. North of Barbados, the dominant water masses have relatively cold temperature and high salinity. These waters are the coldest and saltiest of all. We also detect them close to the continental shelf as a result of coastal upwelling or vertical mixing events (Acquistapace et al., 2022; Olivier et al., 2022). Close to the coast of South America, we find four different water masses with higher SST and a more heterogeneous SSS. Two of them have salinities between 35 and 36 psu. The other two are influenced by the presence of the Amazon freshwater plume, which is advected into the open ocean by the NBC retroreflection and rings. Thus, their salinity ranges from 30 to 33 psu.

Based on measurements of vertical ocean temperature and salinity profiles from gliders, MVPs, CTDs, and uCTDs, we observe that the upper ocean layers coinciding with the freshest water masses have a very different vertical structure than the other four. In particular, they are characterized by a rapid temperature decrease starting above 40 m depth and subsurface warm layers developing between 70 and 80 m depth, while the MLDs are considerably shallower (Figures 3e and 3f). In contrast, the saltier and warmer waters show well mixed vertical profiles with 50 m thick layers of constant density, temperature and salinity (Figures 3c and 3d). Air-sea interface in situ data also show important differences between water masses (Figure 4). For water masses characterized by salinity values below 34 psu, the LHF is systematically lower (Figure 4a). Our results suggest that this is mostly a consequence of increased specific humidity (Figure 4c). ERA5 specific humidity snapshots show that over the Amazon plume, which is not be sampled by SD1064 until late March-April 2020, horizontal advection of moist air from the southeast increases specific humidity. However, other local effects of the air-sea interaction may also be involved. Due to its limited resolution, ERA5 does not reproduce the full range of coupled ocean-atmosphere processes. Therefore, it is not possible to analyze them from the ERA5 output. In the present study, we focus on three different situations where the sampling devices intersect the plume-associated waters to understand the different mechanisms leading to such LHF variations over the different water masses.

The first case consists of the RVs *Atalante* and *Merian* crossing in a very short period of time a cold and salty patch near the coast of Suriname, surrounded by the warm and fresh Amazon plume. This creates a 2°C SST and a 6 psu SSS gradient (Figure 5). The RV *Atalante* MVP vertical profiles (Figures 6b–6d and e) show that the increase of SSS at the plume boundary favors the mixing of subsurface warm layers with the rest of the ML thereby increasing SST and leading to an additional heat release as high as to 35 W m^{-2} locally as seen in Figure 7e. Furthermore, the LHF decomposition shows that SST and wind speed are the two leading factors influencing the change in LHF ($\Delta LHF_U \sim 100$ W m^{-2} and $\Delta LHF_{q_s} \sim 40$ W m^{-2} respectively out of a total of $\Delta LHF \sim 160$ W m^{-2}) as shown in Figure 9. Within the total wind speed influence ($\Delta LHF_U + \Delta LHF_{U,\Delta q}$), the changes in near-surface winds induced by mesoscale (and smaller scale) SST structures (TFB) and near-surface currents (CFB) are on average 10%–30% depending on the water mass (Figure 10). This result is in agreement with previous research using satellite observations and reanalysis (Fernández et al., 2023).

To substantiate these initial case study results, we examine two different time windows during which the Amazon plume-associated water masses are sampled by SD1063 and SD1064. The first occurred between 16th and 19th February 2020, when a weaker (more saline) freshwater plume was transported by the coastal current and the various NBC rings in the region up to 11°N (Figure 11). Although the SST-SSS gradient is much weaker than in the first case (0.4°C - 2.5 psu), we are able to recover the influence of the same mechanisms. Excluding the effect of wetter conditions over the freshest waters (ΔLHF_q), wind speed is the leading variable for LHF changes, followed by SST (Figures 13a and 13b) in agreement with the first case study. Within the total wind speed effect ($\Delta LHF_U + \Delta LHF_{U,\Delta q}$), background wind conditions dominate over both water masses, although the CFB significantly modulates $\Delta LHF_U + \Delta LHF_{U,\Delta q}$ in the freshest waters (Figures 13c and 13d). We also observe a sharp increase of ΔLHF_{q_s} ($\sim$14 W m^{-2}) between 34 and 35 psu as shown in Figure 13e. We hypothesize that this change is due to heat release from the subsurface warm layer heat release, as it is observed in the same salinity range than the first study case and the increase is compatible with Figure 7e. Again, the buoyancy change due to the SSS increase in the plume boundaries enhances the vertical motion and mixes the subsurface warm layers with the rest of the ML. As a result, surface waters become warmer and LHF_{q_s} increases locally. However, we lack data to evaluate this process in more detail, and it remains a research question for modeling studies. Finally, the third study case consists of SD1064 crossing a warm and prominent Amazonian plume between March 31st and 11 April 2020 (Figure 14). The relative importance of the different decomposition terms in the total change of the LHF is consistent with the second case.

The processes described here highlight the complexity of the interactions that drive the changes in the LHF, even during the boreal winter (and spring) when the atmospheric state in the NWTA is relatively stable and the Amazon plume is weak. Also, the ocean structures studied here, such as the NBC rings, last for weeks to months, while the case studies last for a few days, so they can be considered stationary for our purposes. To verify that the mechanisms assessed here are still present and contributing to the overall flux change in the same way, more in situ measurements in other seasons, such as the boreal summer and/or other years, would be highly recommended. They would also be useful for a better understanding of the interannual variability of the LHF. Furthermore, the

influence of the diurnal cycle (which was removed from the beginning) on all the results presented here remains an open research question to be addressed in a future dedicated paper.

This study is limited by the scarcity of data in the region and highlights the importance of collocated ocean, atmosphere, and air-sea interface observations to accurately quantify the various factors influencing heat fluxes and the MABL. As the Amazon plume has only been sampled in three different cases with different background conditions and seasons, more observations of ocean and atmosphere vertical profiles further south, closer to the minimum SSS values of the Amazon River plume, would help us to better quantify its influence on the LHF and heat fluxes in general. In addition, it would be valuable to check how all the mechanisms described above are reproduced in fully coupled regional ocean-atmosphere models and/or high-resolution regional atmospheric models forced with different SST products. In particular, different simulations with different Amazon River plume intensities would be very useful. Even if these simulations are not able to reproduce all the processes included in the observations, they would allow a statistical approach to the problem instead of a case study approach, and thus provide more robust estimates of the contribution of each controlling variable to the change in the LHF.

Appendix A: Further Information on Methodology

A1. Intercomparison Between ERA5 and In Situ SST and Collocation Procedure

Throughout the manuscript, the ERA5 output is collocated with various in situ observations such as Saildrones or TSGs. Following Hall et al. (2022), we use the closest neighbor interpolation technique to match the locations and times of the corresponding in situ product with the nearest location and time available in the ERA5 products. Due to the spatial and temporal resolution of ERA5 (0.25° and 1 hr, respectively), only collocations within this resolution are included. To be consistent with Hall et al. (2022), the closest points in space are collocated before the closest points in time.

However, this operation introduces some inaccuracies in the atmospheric response because ERA5 does not include coupling with the ocean and its resolution is too coarse to detect some of the small-scale ocean features whose effects we are interested in to evaluate (Hersbach et al., 2020). Therefore, the purpose of this subsection is to show how well the ERA5 SST and the TSG SST from Study Cases 1 and 2 agree. The reason for using SST rather than other variables is that mesoscale SST is the ultimate driver of MABLH changes.

The metrics used to compare ERA5 to the in situ observations are the standard deviation of the difference (STD), the mean difference, and the Spearman correlation coefficient. The resulting time series from the collocation are shown in Figure A1 and the statistics in Table A1. We observe from Figure A1a that ERA5 seems to reproduce the SST values and variability quite well (Spearman correlation coefficient of 0.86), since

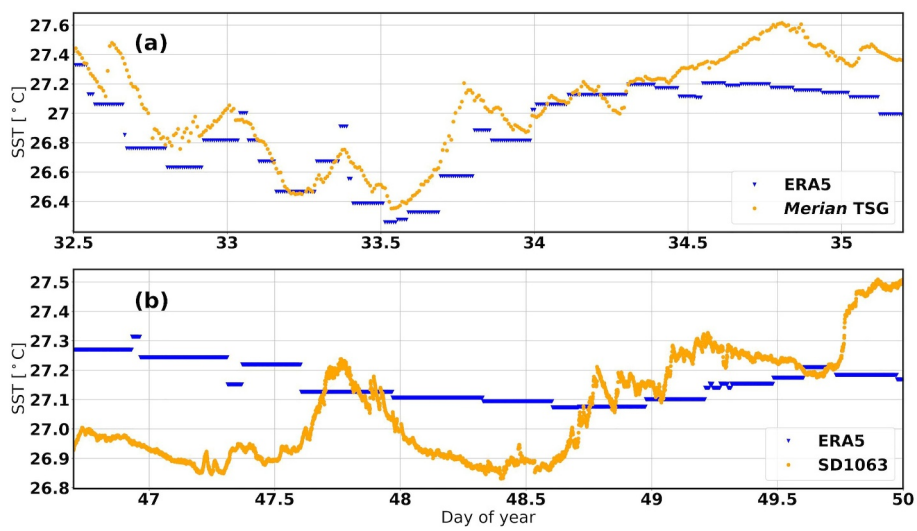

Figure A1. Comparison between the collocated ERA5 SSTs (blue) and (a) the *Merian* TSG SST between the second and the fifth of February 2020 and (b) the SD1063 TSG SST between the 16th and the 19th of February 2020.

Table A1
Mean Difference and Standard Deviation (STD) for ERA5 Minus the Corresponding In Situ Observations, as Well as the Spearman Correlation Coefficient and Its P-Value for Case 1 and Case 2

Metric	Case 1	Case 2
Mean (°C)	−0.17	0.09
STD (°C)	0.15	0.19
Spearman Correlation	0.86	−0.01
p-value	0.00	0.69
Number of samples	389	4,753

Note. The number of samples in both cases is given in the last row.

the *Merian* TSG SST 0.17°C warmer on average. This result, together with the fact that the RSs from the *Atalante* were included in the production of the ERA5 output, encourages us to rely on the ERA5 MABLH values shown in Figure 8d. On the contrary, during the study Case 2, ERA5 is not able to capture either the SST variability or its values, as the Spearman coefficient is close to zero. Nevertheless, the MABLH values shown in Figure 12d seem to reproduce the expected behavior with thicker MABLs in the warm side of the front. Determining the exact causes of this result would require a closer examination of the ERA5 MABLH parameterization and is beyond the scope of this study. What is clear is that ERA5 may not always correctly reproduce MABLH changes, as the forcing itself is not consistent with the observations. However, due to the lack of MABLH observations, we include the ERA5 output in our results.

Given the SST difference between ERA5 and SD1063 in Figure A1b, we also provide a brief discussion of how small a structure we should expect ERA5 to reproduce. Figure A2 shows the SST wavenumber spectra of ERA5 (blue) and SD1063 (gray). Due to its spatial resolution of 0.25°, ERA5 cannot resolve scales smaller than 40 km (the effective spatial resolution). However, SD1063 has a sampling frequency of 1 min, which corresponds to an average sampling interval of 50 m. Thus, it captures the entire mesoscale O (10–200 km) and the submesoscale O (0.1–10 km). Figure A2 also shows the best-fit wavenumber ($k^{-2.8}$) for the submesoscale part of the spectrum. It indicates slightly less energetic submesoscale structures compared to those observed in the Southern Ocean (Swart et al., 2020), but in agreement with other regions of the World Ocean such as the Arctic at 70°N. Overall, the Saildrone measurements confirm the evidence for these submesoscale features already observed in satellite imagery (Olivier et al., 2022).

A2. Diurnal Cycle Removal

This section provides a deeper insight into the methodology used to remove the diurnal cycle in this manuscript (multichannel) singular spectrum analysis (M-SSA) (Ghil et al., 2002; Groth et al., 2017). It is a natural method to extract oscillatory modes of variability from a (multivariate) time series. Here we detail the steps taken for SSA, although the process can be generalized for multiple variables as in Groth et al. (2017). Consider a time series of a

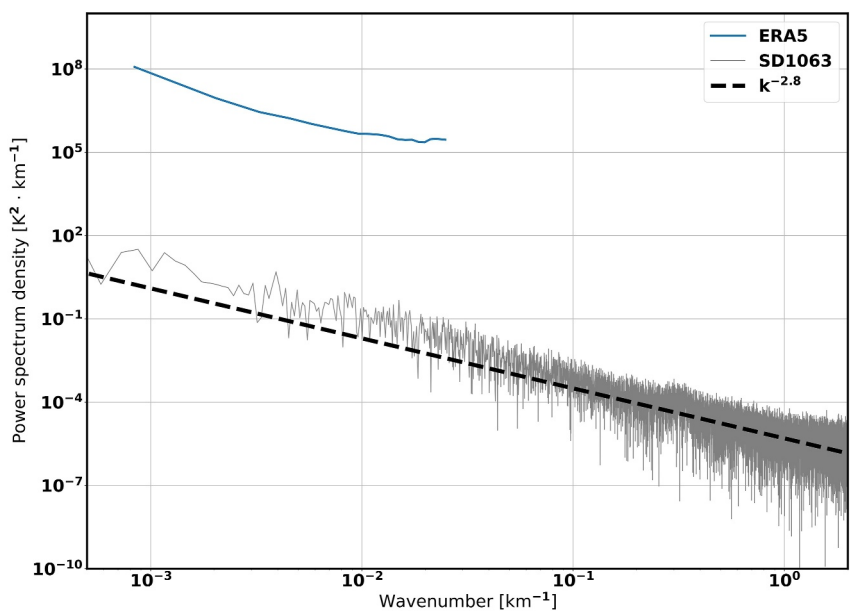

Figure A2. Horizontal SST wavenumber spectra from ERA5 (blue) and SD1063 (gray). The dashed black line is the best-fit slope between 1 and 50 km for SD1063. A log-log plot is used. The SD1063 data were treated as in Swart et al. (2020) before the spectrum was calculated.

variable (SST, near-surface wind, air temperature…) from which we remove the mean and divide by the standard deviation ($\tilde{X}(t)$):

$$\tilde{X}(t) = \{X(t), X(t+1), \ldots X(N)\}. \tag{A1}$$

We want to compute the *lag-covariance* matrix (C) as in Vautard and Ghil (1989) and Ghil et al. (2002). To do this, we first define the *embedded time series* matrix (Y). The general formulation for an element of Y in the *i*th row and *j*th column is

$$y_{i,j} = X(i+j-1). \tag{A2}$$

Following the definition of covariance of a time series with zero mean and unit variance we define C as follows:

$$C = \frac{Y'\ Y}{N} \tag{A3}$$

If we define M as *window size*, only the first N − M + 1 rows of C will be filled with non-zero values. In this manuscript, we choose M equal to 4 days as a compromise. It cannot be too large, because then we would mix information from very different water masses in the diurnal cycle reconstruction, but it also cannot be smaller than 1 day. The choice of N as the normalization factor in Equation 3 is motivated by the fact that $N \gg M$ for all cases in this study. We then diagonalize C to obtain its eigenvectors (ρ_k) and eigenvalues (λ_k) such that

$$C\rho_k = \lambda_k \rho_k. \tag{A4}$$

Projecting the matrix Y onto each eigenvector (ρ_k) yields the corresponding principal component (PC_k):

$$PC_k = Y\rho_k. \tag{A5}$$

These PCs are orthogonal at lag zero, which means that there is no covariance between different PCs. In addition, the variance represented by each PC_k is given by the corresponding eigenvalue λ_k. Finally, one can perform a reconstruction of the variable time series based on a group of PCs (K) such that:

$$RC_{\mathrm{K}}(t) = \frac{1}{M_t} \sum_{k \in \mathrm{K}} \sum_{j=L_t}^{U_t} PC_k(t-j+1)\rho_k(t). \tag{A6}$$

Being the normalization factor (M_t) and the lower and upper bound of summation (L_t and U_t respectively) (Ghil & Vautard, 1991; Vautard et al., 1992):

$$(M_t, L_t, U_t) = \begin{cases} \left(\frac{1}{t}, 1, t\right) & \text{for } 1 \le t \le M-1 \\ \left(\frac{1}{M}, 1, M\right) & \text{for } M \le t \le N-M+1 \\ \left(\frac{1}{N-t+1}, t-N+M, M\right) & \text{for } N-M+2 \le t \le N \end{cases} \tag{A7}$$

Therefore, to remove the diurnal cycle, we compute the various PCs of a given time series with Equation A5. We compute their power spectrum and select those (usually a few) whose dominant period is one day (with a tolerance of ±1 hr) and whose cumulative explained variance is less than 70%. This is a value chosen by the authors to ensure that the PCs representing the diurnal cycle contain an important part of the variance. Therefore, we reconstruct the diurnal cycle using Equation A6 with the selected PCs and the time series without the diurnal cycle with the remaining PCs.

One of the advantages of removing the diurnal cycle in this way, rather than using an averaged diurnal cycle, is that it allows us to recover a space-time varying diurnal cycle, as shown in Figure A3a. We observe that the

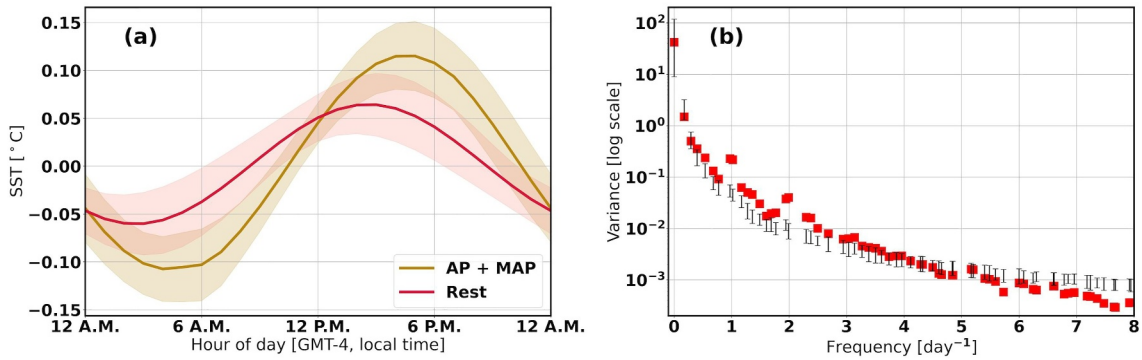

Figure A3. (a) SD1064 SST mean diurnal cycle (solid lines) of the APWs and MAPWs (golden) and the rest of the clusters (crimson) and the corresponding standard deviation (shading). (b) Variance associated to the different PCs of the SD1064 SST time series as a function of their dominant frequency (red squares). The black errorbars denote the 5% and the 95% percentiles of the each PC's variance distribution after repeating the SSA 5000 times assuming the PCs are generated with an AR (1) process.

amplitude of the diurnal SST cycle is larger over the APWs and MAPWs (gold) than over the rest of the water masses (purple). The more shallow the mixed layer is, the easier it is for it to be heated up or cooled down. These spatial variations in the diurnal cycle affect the LHF. For example, if we consider the water masses not associated with the Amazon plume (red curve in Figure A3a), we get a diurnal cycle amplitude of 0.1°C. Assuming a mean wind speed value of 8.5 m s^{-1}, a specific humidity value of 16 g kg^{-1}, an SST of 27°C, and an air temperature of 26.9°C as in Figure 4, we get a 4 W m^{-2} LHF difference between day and night. This difference is a lower bound, since the amplitude of the diurnal SST cycle is larger over plume-associated water masses, and other variables such as wind speed also have a strong diurnal cycle. Furthermore, this LHF difference is already on the order of magnitude of some of the phenomena we are assessing here. Therefore, it is important to remove it before analyzing the in situ observations. The effects of this space-time varying diurnal cycle on the air-sea interface heat fluxes will be further investigated in a future dedicated paper.

Finally, we need to assess whether the diurnal cycles we obtain contain more variance than we would expect if they were generated by noise. Since the PCs are mutually orthogonal, our null hypothesis is that the data were generated by an autoregressive process of order 1: AR (1) (Allen & Smith, 1996). This choice is also motivated by the fact that AR (1) processes are incapable of supporting the oscillatory behavior we are interested in detecting. After formulating the null hypothesis, we generate a large ensemble of surrogate data segments (5,000 realizations of the noise model consisting of a generic AR (1) process) with the same length as $\tilde{X}(t)$. We compute the variance associated with the PCs of each realization as before. The resulting 5% and 95% percentiles of the variance distribution from the surrogate data segments are shown as error bars in Figure A3b, and the variances associated with the PCs derived from $\tilde{X}(t)$ are the red squares. We observe that there is a pair of PCs at a 1 day period that lie above their surrogate data bars, corresponding to a statistically significant diurnal cycle.

To know which variables we need to remove the diurnal cycle from, we run the significance test on the time series of each variable and assess whether or not the daily peaks are above the surrogate distribution. Table A2 contains the list of variables and devices from which the diurnal cycle is removed. For ARTHUS and DLs, we apply M-SSA, which is a generalization of SSA for variables with more than one dimension (in this case, time and altitude).

Table A2
List of Variables and Devices From Which the Diurnal Cycle Is Removed and Methodology Based Upon the AR (1) Test

Variable(s)	Instrument(s)	Methodology
SST, RH_{2m}, u_{5m}, v_{5m}, T_{2m}	Saildrones (NASA + NOAA)	SSA
SST, RH_{2m}, u_{5m}, v_{5m}, T_{2m}	RV *Atalante* mast	SSA
u, *v*, w, WVMR	ARTHUS and DLs	M-SSA

Note. Surface pressure from Saildrones and the RV *Atalante* mast had a very prominent semi-Diurnal peak which was also removed.

Finally, the diurnal cycle is not removed from the vertical ocean profiles because the data are not equally spaced in time. This is one of the shortcomings of this study.

A3. MABLH Computation From RSs

Here we compare three different methods to compute the MABLH from the RSs, as there is no universal technique for handling RS data. Before calculating the MABLH, we first perform a linear interpolation to all vertical profiles to fill in missing values. Then, we smooth the air temperature, winds, and surface water vapor mixing ratio using a five-point running average (equivalent to 50 m in height) as in Hande et al. (2012) or Peng et al. (2023). We perform this operation to remove small scale features in the vertical profiles that could lead to spurious MABLH values. We also ignore the first 200 m of the atmosphere in all calculations. This is to avoid the influence of the surface layer and the fast and erratic movements of the RS after deployment.

First, we use the Richardson bulk number (Ri_B) method proposed by (Vogelezang & Holtslag, 1996). Ri_B is defined, for a given height, as the ratio of the turbulence associated with the vertical temperature gradient to the turbulence generated by wind shear. In this paper we ignore the effects of surface friction in the calculation of Ri_B. Thus, according to (Seidel et al., 2012) we have

$$Ri_B = \frac{\left[\frac{g}{\theta_{vs}}\right][\theta_{vz} - \theta_{vs}]\,[z - z_s]}{(u_z - u_s)^2 + (v_z - v_s)^2}, \tag{A8}$$

where θ_v is the virtual potential temperature and u and v are the zonal and meridional wind components. The subscripts "s" denote the values of the variables at a reference level (z_s) that we choose to be closest to the surface. Thus, the MABLH is the lowest level at which Ri_B exceeds 0.25, as in Davison et al. (2013) and Seidel et al. (2012).

Second, we try the virtual potential temperature gradient $\left(\frac{d\theta_v}{dz}\right)$ method (or parcel method) from Hande et al. (2012). We estimate it with central differences, and the derivatives along the edges are computed with one-sided differences. The MABLH is then estimated as the absolute maximum of the gradient between 200 and 1,200 m. We impose a lower bound on the gradient to ensure that the main inversion is greater than 0.01 K-m^{-1}. This is the case for 99% of the profiles.

Finally, we consider a slight modification of the virtual potential temperature gradient method. To ensure that the potential temperature inversion at the top of the MABL is maintained in height, we first find the height level at which the difference between the local $\frac{d\theta_v}{dz}$ and the mean of all $\frac{d\theta_v}{dz}$ below it exceeds two standard deviations from the distribution formed by all $\frac{d\theta_v}{dz}$ below the given height level. If this condition is met in three consecutive levels, we consider the MABLH to be the mean of the above three levels.

Figure A4 shows the vertical structure of the atmosphere at different locations in the time period of Case 1 (each one in a row). The first location (Figures A4a, A4b, and A4c) shows that when there is a well-mixed MABL with constant θ_v and then a decrease at the top of the MABL, the parcel method and the modified parcel method give similar MABLH values (Figure A4b). On the contrary, the Ri_B method shown in Figure A4c gives an unrealistically low MABLH value of little more than 200 m. In fact, the Ri_B method is strongly affected by the high wind shear values usually found near the surface (Figure A4a), even if the θ_v vertical profile remains homogeneous. This fact could also explain the MABLH values around 200 m for the cold side of the front observed by Acquistapace et al. (2022). Since θ_v is mostly constant up to 1 km, we discard the Ri_B method to compute the MABLH.

At the second location (Figures A4d, A4e, and A4f) we observe that the parcel method gives a MABLH of 850 m (Figure A4e), which coincides with the Ri_B value (Figure A4f) associated with a peak in wind shear at the same height (Figure A4d). However, from the θ_v vertical profile we can observe that the well-mixed MABLH reaches 600 m, as indicated by the black line representing the modified parcel algorithm value. In fact, the parcel method fails to provide a correct value of MABLH when there are multiple inversions in the θ_v profile.

Even when there is a single inversion, the parcel method can slightly overestimate the MABLH, as we observe in the third location (Figures A4g, A4h, and A4i). Figure A4h shows a MABLH slightly above the start of the θ_v inversion. In this case, the Ri_B method also overestimates the MABLH Figure A4i. Therefore, we choose the modified parcel method to estimate the MABLH from RSs.

We are aware that we should be cautious when estimating the MABLH with RSs because they are very sensitive to wind speed measurements. Wind speed is subject to significant sampling error and the effects of wave-like disturbances. In addition, cold pools can invalidate almost any scheme. In our case, this should not be a problem. Between the second and the 5^{5th} of February 2020, there were no cold pool conditions, as shown by the yellow dots in Figure 9a in Touzé-Peiffer et al. (2022).

A4. Extended Analysis of the Atmospheric Vertical Profiles From RSs and ERA5

In Figures 8a–8c we show the mean vertical profiles of horizontal wind speed, vertical wind speed and specific humidity from ARTHUS and the DLs to assess the atmospheric response in the first case study. In this section we

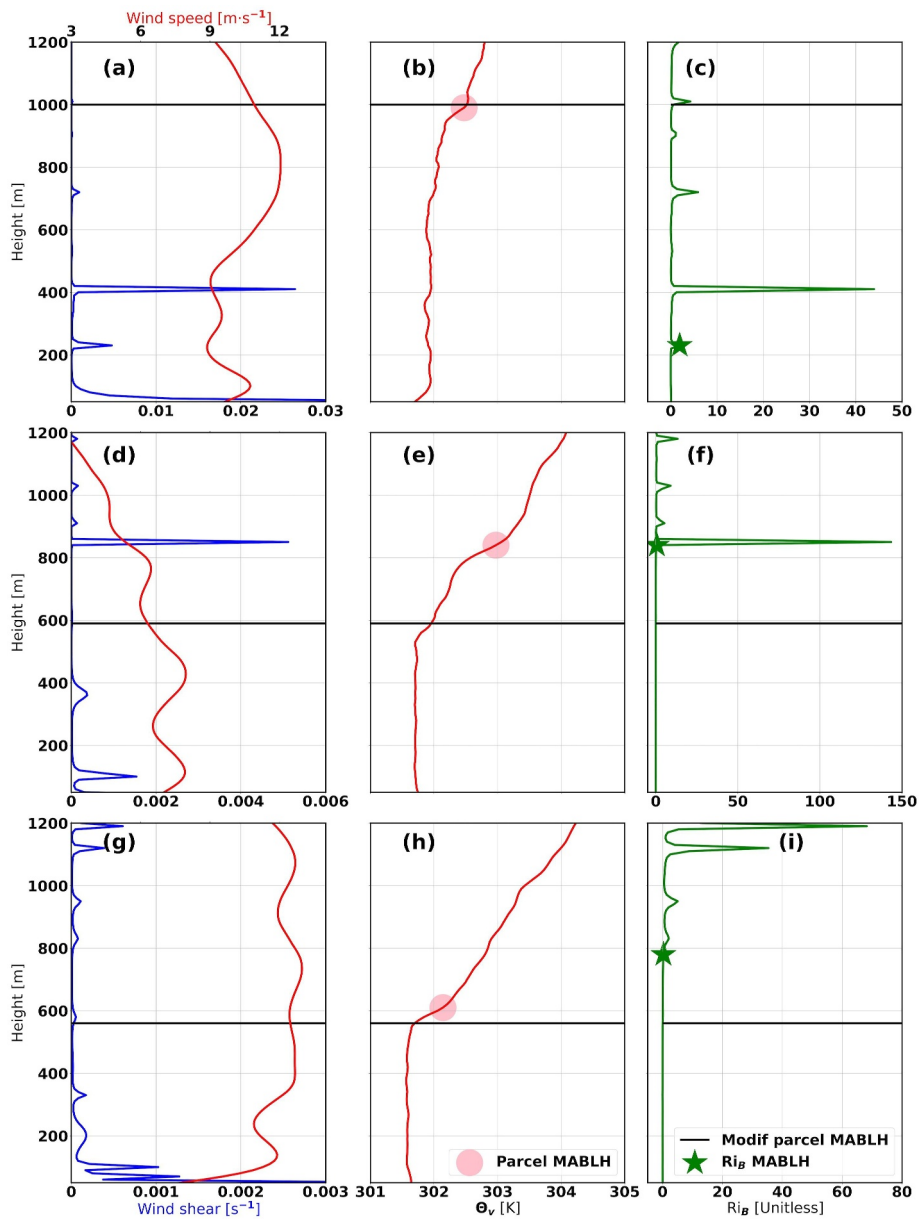

Figure A4. (a), (d), and (g) show the RS vertical profiles of wind shear (blue) and wind speed (red). (b), (e) and (h) show θ_v vertical profiles (pink line) and MABLH values from the gradient (parcel) method (pink circles). (c), (f) and (i) show the Ri_B vertical profiles (green) and the MABLH computed by the Ri_B method (green stars). In all panels, the horizontal black line represents the MABLH calculated with the modified parcel method. Each panel row corresponds to a different location.

include the mean vertical profiles of horizontal wind speed and specific humidity from the RSs and collocated ERA5 (Figure A5).

The atmospheric wind speed response of the *Atalante* RSs (Figure A5a) is similar to that of the DLs. Weaker wind speeds dominate over the cold side of the front (cyan). However, there is a large spread and overlap between the profiles, probably due to the reduced number of observations (#15 here as opposed to #96 for the DLs). This larger spread is also associated with the broad RS MABLH PDFs in Figure 8d. Note also that the wind speed values are significantly larger than those shown in Figure 8d. The vertical profiles of specific humidity are shown in Figure A5b and show that drier conditions predominate over the cold side of the front. Again, the overlap between the warmest and coldest profiles is very important.

The ERA5 horizontal wind response shows the same tendency as those from the observations (RSs and DL/ARTHUS) as shown in Figure A5c. Higher wind speeds are observed over the warm side of the front and reduced winds dominate over the cold side, with little overlap between the vertical profiles. The vertical specific humidity profiles in Figure A5d show that a much moister MABL is expected over the warm side of the front, in contrast to the ARTHUS humidity profiles (Figure 8c).

In summary, while ERA5 seems to correctly reproduce SST values and variability (Figure A1a), its atmospheric response does not match that of the observations with respect to specific humidity. We hypothesize that the possible misrepresentation of MABL air-sea interaction processes in ERA5 could lead to unsatisfactory atmospheric vertical structures. We should always keep these divergences in mind when comparing ERA5 with in situ observations.

A5. Numerical and Analytical LHF Decomposition

Following Tanimoto et al. (2003), Chuda et al. (2008), and Yang et al. (2016), we apply a Reynolds decomposition to the near-surface wind speed, saturation specific humidity, and specific humidity, which we denote generically as X

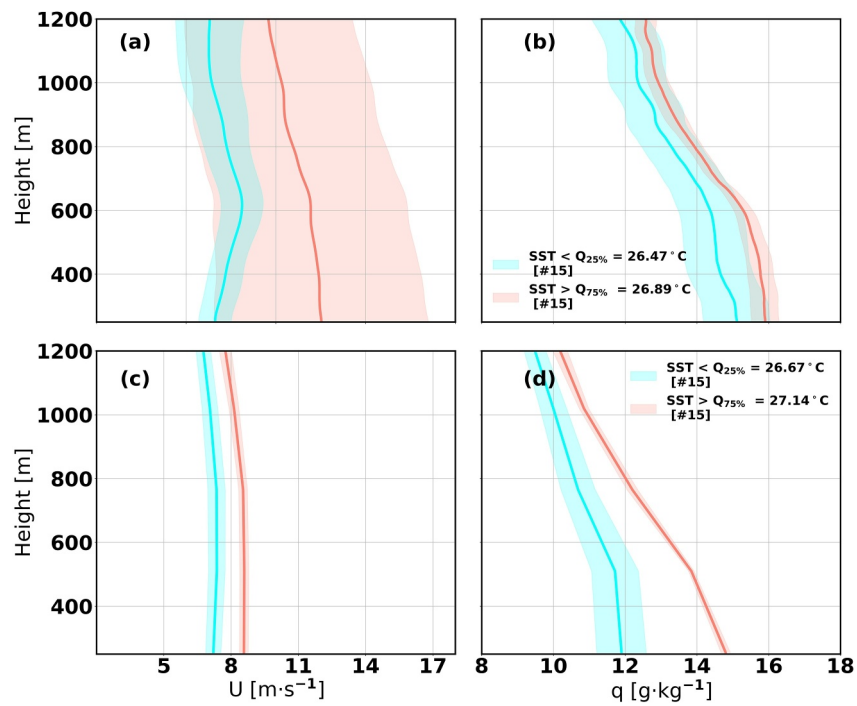

Figure A5. Mean vertical profiles (solid lines) and standard deviations (shading) of (a) *Atalante* RS horizontal wind speed, (b) RS specific humidity, (c) ERA5 collocated horizontal wind speed, and (d) ERA5 collocated specific humidity. As in Figure 8, the profiles are obtained from the warmest and coldest SST 25% percentiles and are color-coded according to their mode clusters.

$$X = \overline{X} + \Delta X, \tag{A9}$$

where $\overline{X}$ is the time mean averaged over the time period of each study case and ΔX is the anomaly with respect to that mean from each value in the time series. We then consider the mass formula for LHF from COARE3.5:

$$LHF = \rho_a \, L_e \, C_e \, U \, (q_s - q), \tag{A10}$$

where ρ_a is the air density, L_e is the latent heat of evaporation, and C_e is the moisture exchange coefficient. Considering these three parameters as constants and applying Equation A9 to the rest of the variables in Equation A10 we obtain:

$$LHF = \rho_a \, L_e \, C_e \left[\overline{U}\overline{q_s} + \Delta U\overline{q_s} + \overline{U}\Delta q_s + \Delta U\Delta q_s - \overline{U}\overline{q} - \Delta U\overline{q} - \overline{U}\Delta q - \Delta U\Delta q\right] \tag{A11}$$

Averaging Equation A11 we get:

$$\overline{LHF} = \rho_a \, L_e \, C_e \left[\overline{U}\,(\overline{q_s} - \overline{q}) + \cancelto{0}{\overline{\Delta U\,(\Delta q_s - \Delta q)}}\right] = \rho_a \, L \, C_e \left[\overline{U}\overline{q_s} - \overline{U}\overline{q}\right] \tag{A12}$$

Therefore

$$\Delta LHF = LHF - \overline{LHF} = \rho_a \, L_e \, C_e \left[\Delta U\overline{q_s} + \overline{U}\Delta q_s + \Delta U\Delta q_s - \Delta U\overline{q} - \overline{U}\Delta q - \Delta U\Delta q\right] \tag{A13}$$

which is Equation A12 except for the residual to ensure that the LHF budget is closed. We also tested the numerical first-order Taylor series deconvolution approach as in Kwiatkowski and Orr (2018) to see if we could reduce the residual. In this case, a given LHF anomaly (ΔLHF) is expressed as

$$\Delta LHF = \underbrace{\left(\frac{\partial LHF}{\partial U}\right)\Delta U}_{\Delta \mathrm{LHF_{wspd}}} + \underbrace{\left(\frac{\partial LHF}{\partial q}\right)\Delta q}_{\Delta \mathrm{LHF_{qair}}} + \underbrace{\left(\frac{\partial LHF}{\partial T}\right)\Delta T}_{\Delta \mathrm{LHF_{tair}}} + \underbrace{\left(\frac{\partial LHF}{\partial SST}\right)\Delta SST}_{\Delta \mathrm{LHF_{SST}}} + \mathrm{Residual}, \tag{A14}$$

where the partial differentials are estimated numerically as the slope of the regression between LHF and the corresponding variable, holding the other variables constant at their mean values for the study case period. ΔU, Δq, ΔT, and ΔSST are changes in the input variables (wind speed, specific humidity, air temperature, and sea surface temperature, respectively) synchronized with ΔLHF. They are also computed with respect to the mean time period of the study case. Residual is a term necessary to close the LHF budget due to numerical errors in performing the partial derivatives.

The results of the numerical Taylor deconvolution are shown in Figure A6. In comparison with Figure 9, the contributions of wind speed and specific humidity (Figures 9b and A6d; Figures 9d and A6c) are very similar. In addition, the changes in SST are represented by the q_s in the analytical decomposition (Figure 9c), which is similar to the pattern of Figure A6e. The residuals of the two decompositions (Figures 9f and A6f) have the same order of magnitude, with the Taylor decomposition (Figure A6f) being slightly smaller. Perhaps this is a consequence of the fact that the error associated with the averaging of C_e, L and ρ_a (which depend on the air temperature) is separated in $\Delta \mathrm{LHF}_T$ (Figure A6d) and not isolated in the numerical decomposition.

Although the residual is slightly smaller in the numerical first-order Taylor decomposition, we use the analytical method throughout the main text to avoid numerical errors. It also allows us to interpret the various terms of the LHF budget in a simpler and more straightforward manner.

A6. Residual Term and Influence of the MABL Stability

The residual term in Equation A12 is shown in Figures 9f, 13a, 13b, and 15c. From these figures we conclude that the residual is generally a second-order contribution, as it is smaller than the first-order terms $\Delta \mathrm{LHF}_U$ and LHF_{q_s} in

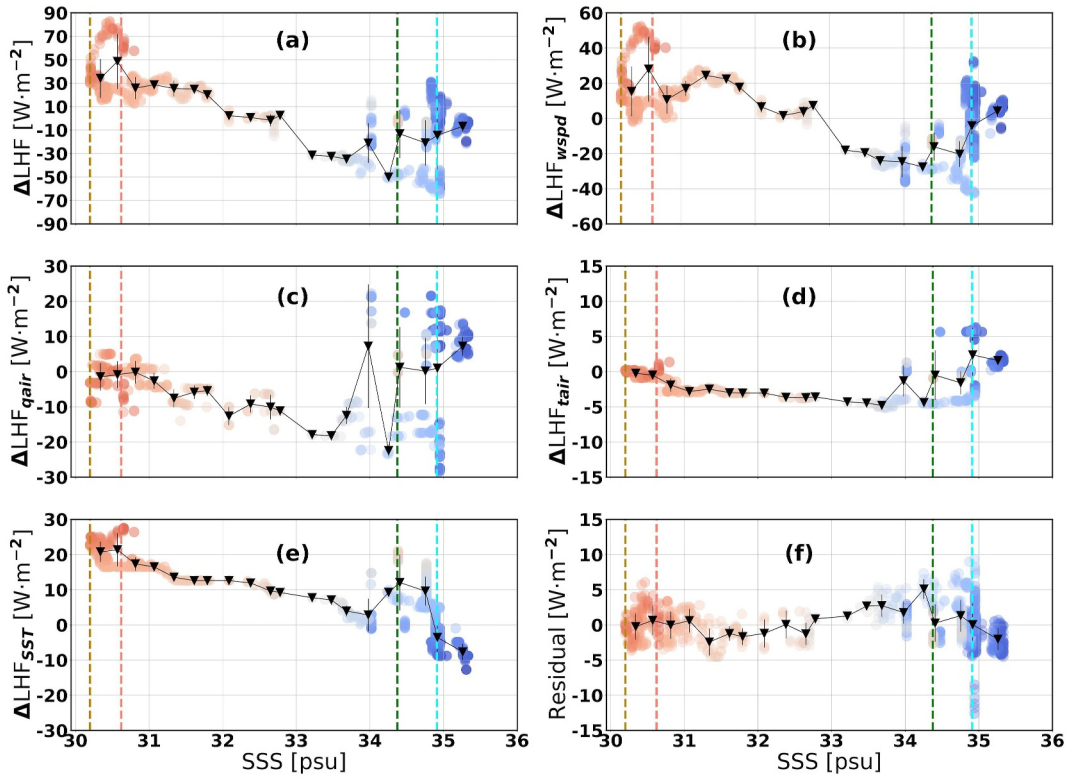

Figure A6. As in Figure 9 but for the numerical Taylor deconvolution. (a) Represents the total change in ΔLHF, (b) ΔLHF_{wspd}, (c) ΔLHF_{q}, (d) ΔLHF_{T}, (e) ΔLHF_{SST} and (f) Residual. The colors in the markers denote RV *Atalante* TSG SST values with the same color scale as in Figures 7 and 9.

most cases. However, at certain locations (between 34 and 35 psu in Figure 9f) it becomes comparable to the leading order terms. This point is discussed in this section.

The residual comes from the fact that we are averaging the coefficients preceding the bulk formula (Equation A12) over the different time periods of the cases studied. These constants are the air density (ρ_a), the latent heat of evaporation (L_e), and the moisture exchange coefficient (C_e). In COARE3.5 (Edson et al., 2013), ρ_a depends on air temperature, pressure, and humidity, L_e on SST and SSS, and C_e on the stability of the atmospheric column via the MOST. We plot these parameters together for the first study case with the difference between air temperature and SST as a proxy for MABL stability in Figure A7.

We observe that C_e (L_e and $T - SST$) decrease (increase) monotonically with increasing salinity from 30 to 34 psu. However, between 34 and 35 psu these parameters show a larger spread and the above trends are no longer followed. In particular, from the SST values represented by the colors of the markers, it is interesting to see that we have unstable ($T - SST \leq 0$) MABLs, which translate into larger values of C_e and ρ_a. This change in atmospheric stability, influenced by air temperature and wind variations, is responsible for the high residual values shown in Figure 9f and the erratic behavior of ΔLHF_q in Figure 9d as well.

Therefore, the stability of the MABL also affects the spatio-temporal variations of the LHF. In our study, its influence is contained in the residual term of the decomposition, since the coefficients preceding the bulk formula are averaged and considered as constants. In the majority of cases, this averaging is a good approximation, as the residual turns out to be smaller than the rest of the terms in Equation A12. However, in regions with strong changes in atmospheric stratification, the residual becomes important and should be considered in the analyses.

A7. Importance of Considering Surface Currents When Computing LHF

Surface currents influence LHF in two ways.

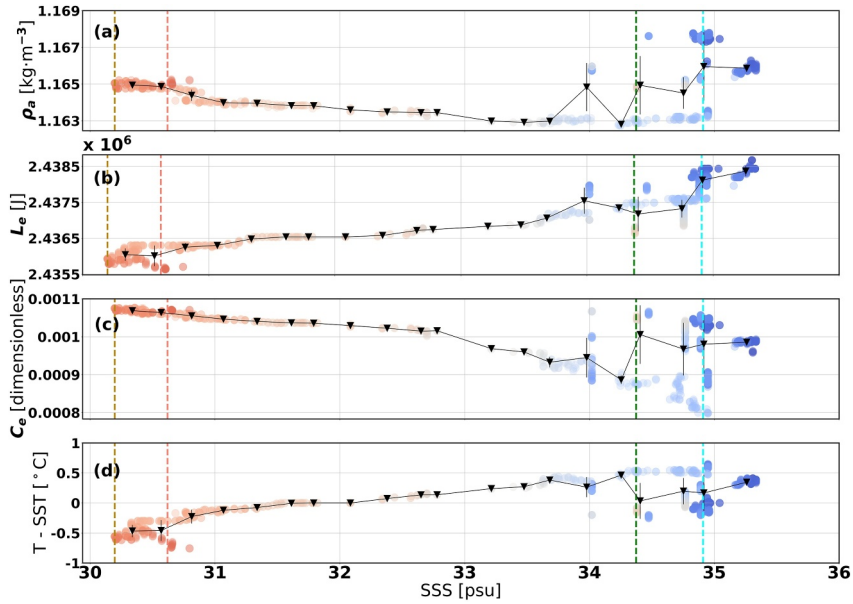

Figure A7. As in Figure 9 but for the coefficients in Equation A12. (a) Represents ρ_a, (b) L_e, (c) C_e and (d) T-SST. The colors in the markers denote RV *Atalante* TSG SST values with the same color scale as in Figures 7 and 9.

- Via the relative winds: to calculate LHF, we use relative surface winds with respect to ocean currents (surface winds minus surface currents) instead of just surface winds.
- Via current feedback (CFB). Surface currents induce a momentum transfer from the ocean to the atmosphere, which modifies the surface winds and thus the LHF. This momentum transfer is quantified by the coupling coefficient shown in Equation A13.

To test the effect of both phenomena on the LHF, Figure A8 shows in blue the relative error between the LHF computed from surface winds (LHF_{wspd}) and the LHF computed using relative winds ($LHF_{wspd_{rel}}$). The orange

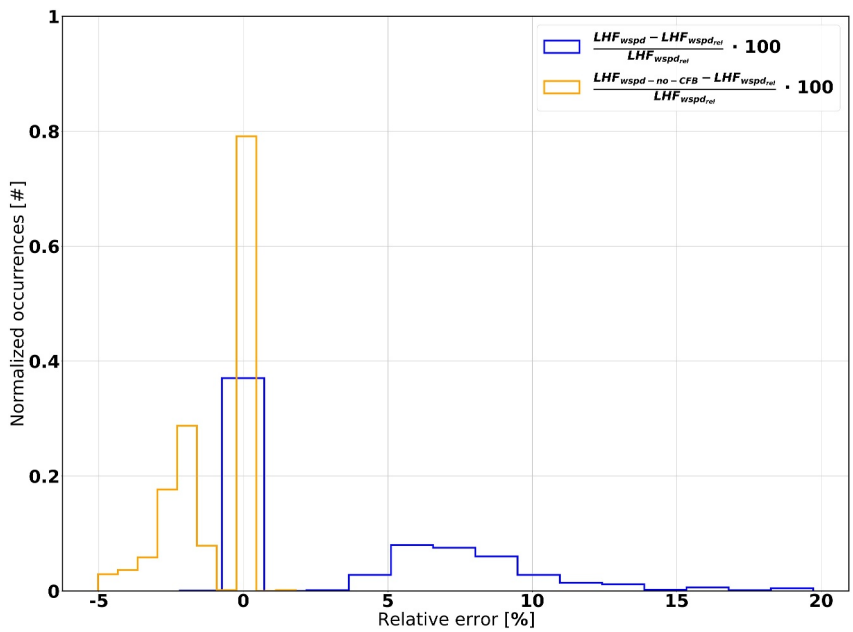

Figure A8. Blue: Histogram of the relative error between the LHF computed with surface winds only (LHF_{wspd}) and the LHF computed with relative winds (LHF_{rel}). Orange: Histogram of the relative error between LHF computed without CFB effects ($LHF_{wspd-no-CFB}$) and LHF computed with relative winds. This figure corresponds to the first case study.

histogram represents the difference between the LHF computed without the CFB effect but using relative winds ($LHF_{wspd-no-CFB}$) and the LHF computed using relative winds. Ignoring relative winds in the LHF calculation can result in a relative error of 20%. The CFB effect in turn causes relative errors ranging from 0% to −5%. Therefore, both phenomena must be taken into account in order to obtain accurate LHF values. Not only because this allows for more accurate estimates of LHF, but also because they induce errors of the same order of magnitude as other effects we evaluate here, such as subsurface warm layer heat release or even thermal feedback (TFB).

A8. Table of Acronyms

Table A3
List of Acronyms by Order of Appearance

Acronym	Meaning
LHF	Latent heat flux
NWTA	North-west tropical Atlantic
SST	Sea-surface temperature
NBC	North-Brazil current
SSS	Sea-surface salinity
ML	Mixed layer
BL	Barrier layer
DMM	Downward momentum mixing
PA	Pressure adjustment
MABL	Marine atmospheric boundary layer
MABLH	Marine atmospheric boundary layer height
TFB	Thermal feedback
CFB	Current feedback
RV	Research vessel
CTD	Conductivity temperature and depth (device)
uCTD	Underway CTD
MVP	Moving vessel profiler
TSG	Thermosalinograph
RS	Radiosondes
WVMR	Water vapor mixing ratio
ARTHUS	Atmospheric Raman temperature and humidity sounder
BR	Backscatter ratio
DL	Doppler lidar
ADCP	Acoustic Doppler current profiler
RH	Relative humidity
ADT	Absolute dynamic topography
(M-)SSA	(Multi channel-) singular spectrum analysis
MLD	Mixed layer depth
BLT	Barrier layer thickness
OHC	Ocean heat content
MOST	Monin-Obukhov similarity theory
CBH	Cloud base height
NASW	North Atlantic subtropical waters

Table A3
Continued

Acronym	Meaning
RWs	Retroflection waters
MRWs	Modified retroflection waters
GCWs	Green cluster waters
CCWs	Cyan cluster waters
APWs	Amazon plume waters
MAPWs	Modified Amazon plume waters
PDF	Probability density function
STD	Standard deviation of the difference
PC	Principal component
AR (1)	Autorregressive process of order 1

Data Availability Statement

We benefited from numerous data sets made freely available and listed here.

- All the in situ measurements taken from the 4 RVs and the autonomous vehicles (Saildrones, ARGO or gliders) (Bony & Bjorn, 2021): https://observations.ipsl.fr/aeris/eurec4a/
- SeaFlux (Roberts et al., 2020), http://dx.doi.org/10.5067/SEAFLUX/DATA101
- ERA5 (Hersbach et al., 2020), https://cds.climate.copernicus.eu/cdsapp#!/data%20set/reanalysis-era5-single-levels?tab=form
- MUR-JPL (Chin et al., 2017) , https://thredds.jpl.nasa.gov/thredds/ncss/grid/OceanTemperature/MUR-JPL-L4-GLOB-v4.1.nc/dataset.html
- SMAP maps produced by Remote Sensing System (RSS v4 40 km) (Boutin et al., 2021) https://doi.org/10.5285/5920a2c77e3c45339477acd31ce62c3c
- Global Ocean Gridded *L* 4 Sea Surface Heights And Derived Variables Reprocessed 1,993 Ongoing (CLS, 2018). https://doi.org/10.48670/moi-00148.
- ETOPO2 seafloor depth (Smith & Sandwell, 1997), https://sos.noaa.gov/catalog/data%20sets/etopo2-topography-and-bathymetry-natural-colors/

Acknowledgments
The authors gratefully acknowledge the support of MERCATOR OCEAN as well as the contributions from Drs. Meghan Cronin and Samantha Wills from NOAA. We also warmly thank the captain and crew of RVs *Atalante*, *Merian*, *Meteor* and *Ronald H. Brown*.

References

Acquistapace, C., Meroni, A. N., Labbri, G., Lange, D., Späth, F., Abbas, S., & Bellenger, H. (2022). Fast atmospheric response to a cold oceanic mesoscale patch in the north-western tropical atlantic. *Journal of Geophysical Research: Atmospheres*, *127*(21), e2022JD036799. https://doi.org/10.1029/2022jd036799

Allen, M. R., & Smith, L. A. (1996). Monte Carlo ssa: Detecting irregular oscillations in the presence of colored noise. *Journal of Climate*, *9*(12), 3373–3404. https://doi.org/10.1175/1520-0442(1996)009<3373:mcsdio>2.0.co;2

Anderson, S. P., Weller, R. A., & Lukas, R. B. (1996). Surface buoyancy forcing and the mixed layer of the western pacific warm pool: Observations and 1d model results. *Journal of Climate*, *9*(12), 3056–3085. https://doi.org/10.1175/1520-0442(1996)009<3056:sbfatm>2.0.co;2

Andrade-Canto, F., & Beron-Vera, F. (2022). Do eddies connect the tropical atlantic ocean and the gulf of Mexico? *Geophysical Research Letters*, *49*(20), e2022GL099637. https://doi.org/10.1029/2022gl099637

Balaguru, K., Chang, P., Saravanan, R., Leung, L. R., Xu, Z., Li, M., & Hsieh, J.-S. (2012). Ocean barrier layers' effect on tropical cyclone intensification. *Proceedings of the National Academy of Sciences*, *109*(36), 14343–14347. https://doi.org/10.1073/pnas.1201364109

Bishop, S. P., Small, R. J., Bryan, F. O., & Tomas, R. A. (2017). Scale dependence of midlatitude air–sea interaction. *Journal of Climate*, *30*(20), 8207–8221. https://doi.org/10.1175/jcli-d-17-0159.1

Bony, S., & Bjorn, S. (2021). Eurec4a operational center. Retrieved from https://observations.ipsl.fr/aeris/eurec4a/

Boutin, J., Vergely, J., Reul, N., Catany, R., Koehler, J., & Martin, A. (2021). Esa sea surface salinity climate change initiative (sea_surface_salinity_cci): Weekly and monthly sea surface salinity products, v03. 21, for 2010 to 2020 [Dataset]. *CEDA*. https://doi.org/10.5285/5920a2c77e3c45339477acd31ce62c3c

Breugem, W.-P., Chang, P., Jang, C., Mignot, J., & Hazeleger, W. (2008). Barrier layers and tropical atlantic sst biases in coupled gcms. *Tellus A: Dynamic Meteorology and Oceanography*, *60*(5), 885–897. https://doi.org/10.3402/tellusa.v60i5.15505

Buck, A. L. (1981). New equations for computing vapor pressure and enhancement factor. *Journal of Applied Meteorology and Climatology*, *20*(12), 1527–1532. https://doi.org/10.1175/1520-0450(1981)020<1527:nefcvp>2.0.co;2

Bye, J. A. (1985). Chapter 6 large-scale momentum exchange in the coupled atmosphere-ocean. *Coupled Ocean-Atmosphere Models*. https://doi.org/10.1016/s0422-9894(08)70702-5

Chelton, D. B., Esbensen, S. K., Schlax, M. G., Thum, N., Freilich, M. H., Wentz, F. J., et al. (2001). Observations of coupling between surface wind stress and sea surface temperature in the eastern tropical pacific. *Journal of Climate*, *14*(7), 1479–1498. https://doi.org/10.1175/1520-0442(2001)014<1479:oocbsw>2.0.co;2

Chen, Y., Speich, S., & Laxenaire, R. (2022). Formation and transport of the south atlantic subtropical mode water in eddy-permitting observations. *Journal of Geophysical Research: Oceans*, *127*(1), e2021JC017767. https://doi.org/10.1029/2021jc017767

Chin, T. M., Vazquez-Cuervo, J., & Armstrong, E. M. (2017). A multi-scale high-resolution analysis of global sea surface temperature [Dataset]. *Remote Sensing of Environment*, *200*, 154–169. https://doi.org/10.1016/j.rse.2017.07.029

Chuda, T., Niino, H., Yoneyama, K., Katsumata, M., Ushiyama, T., & Tsukamoto, O. (2008). A statistical analysis of surface turbulent heat flux enhancements due to precipitating clouds observed in the tropical western pacific. *Journal of the Meteorological Society of Japan. Ser. II*, *86*(3), 439–457. https://doi.org/10.2151/jmsj.86.439

CLS. (2018). Global ocean gridded l 4 sea surface heights and derived variables reprocessed 1993 ongoing [Dataset]. https://doi.org/10.48670/moi-00148

Dai, A., & Trenberth, K. E. (2002). Estimates of freshwater discharge from continents: Latitudinal and seasonal variations. *Journal of Hydrometeorology*, *3*(6), 660–687. https://doi.org/10.1175/1525-7541(2002)003<0660:eofdfc>2.0.co;2

Davison, J. L., Rauber, R. M., Di Girolamo, L., & LeMone, M. A. (2013). A revised conceptual model of the tropical marine boundary layer. part i: Statistical characterization of the variability inherent in the wintertime trade wind regime over the western tropical atlantic. *Journal of the Atmospheric Sciences*, *70*(10), 3005–3024. https://doi.org/10.1175/jas-d-12-0321.1

de Boyer Montégut, C., Madec, G., Fischer, A. S., Lazar, A., & Iudicone, D. (2004). Mixed layer depth over the global ocean: An examination of profile data and a profile-based climatology. *Journal of Geophysical Research*, *109*(C12). https://doi.org/10.1029/2004jc002378

de Boyer Montégut, C., Mignot, J., Lazar, A., & Cravatte, S. (2007). Control of salinity on the mixed layer depth in the World Ocean: 1. General description. *Journal of Geophysical Research*, *112*(C6). https://doi.org/10.1029/2006jc003953

Didden, N., & Schott, F. (1993). Eddies in the north Brazil current retroflection region observed by geosat altimetry. *Journal of Geophysical Research*, *98*(C11), 20121–20131. https://doi.org/10.1029/93jc01184

Donlon, C., Robinson, I., Casey, K., Vazquez-Cuervo, J., Armstrong, E., Arino, O., et al., (2007). The global ocean data assimilation experiment high-resolution sea surface temperature pilot project. *Bulletin of the American Meteorological Society*, *88*(8), 1197–1214. https://doi.org/10.1175/bams-88-8-1197

Edson, J. B., Jampana, V., Weller, R. A., Bigorre, S. P., Plueddemann, A. J., Fairall, C. W., et al. (2013). On the exchange of momentum over the open ocean. *Journal of Physical Oceanography*, *43*(8), 1589–1610. https://doi.org/10.1175/jpo-d-12-0173.1

Fairall, C. W., Bradley, E. F., Hare, J., Grachev, A. A., & Edson, J. B. (2003). Bulk parameterization of air–sea fluxes: Updates and verification for the coare algorithm. *Journal of Climate*, *16*(4), 571–591. https://doi.org/10.1175/1520-0442(2003)016<0571:bpoasf>2.0.co;2

Fairall, C. W., Bradley, E. F., Rogers, D. P., Edson, J. B., & Young, G. S. (1996). Bulk parameterization of air-sea fluxes for tropical ocean-global atmosphere coupled-ocean atmosphere response experiment. *Journal of Geophysical Research*, *101*(C2), 3747–3764. https://doi.org/10.1029/95jc03205

Fernández, P., Speich, S., Borgnino, M., Meroni, A. N., Desbiolles, F., & Claudia, P. (2023). On the importance of the atmospheric coupling to the small-scale ocean in the modulation of latent heat flux. *Frontiers in Marine Science*, *10*, 1136558. https://doi.org/10.3389/fmars.2023.1136558

Foltz, G. R., & McPhaden, M. J. (2009). Impact of barrier layer thickness on sst in the central tropical north atlantic. *Journal of Climate*, *22*(2), 285–299. https://doi.org/10.1175/2008jcli2308.1

Fournier, S., Chapron, B., Salisbury, J., Vandemark, D., & Reul, N. (2015). Comparison of spaceborne measurements of sea surface salinity and colored detrital matter in the amazon plume. *Journal of Geophysical Research: Oceans*, *120*(5), 3177–3192. https://doi.org/10.1002/2014jc010109

Foussard, A., Lapeyre, G., & Plougonven, R. (2019). Response of surface wind divergence to mesoscale sst anomalies under different wind conditions. *Journal of the Atmospheric Sciences*, *76*(7), 2065–2082. https://doi.org/10.1175/jas-d-18-0204.1

Fratantoni, D. M., & Glickson, D. A. (2002). North Brazil current ring generation and evolution observed with seawifs. *Journal of Physical Oceanography*, *32*(3), 1058–1074. https://doi.org/10.1175/1520-0485(2002)032<1058:nbcrga>2.0.co;2

Fratantoni, D. M., & Richardson, P. L. (2006). The evolution and demise of north Brazil current rings. *Journal of Physical Oceanography*, *36*(7), 1241–1264. https://doi.org/10.1175/jpo2907.1

Frenger, I., Gruber, N., Knutti, R., & Münnich, M. (2013). Imprint of southern ocean eddies on winds, clouds and rainfall. *Nature Geoscience*, *6*(8), 608–612. https://doi.org/10.1038/ngeo1863

Garraffo, Z. D., Johns, W. E., Chassignet, E. P., & Goni, G. J. (2003). North Brazil Current rings and transport of southern waters in a high resolution numerical simulation of the North Atlantic. *Interhemispheric Water Exchange in the Atlantic Ocean*, *68*, 375–409. https://doi.org/10.1016/s0422-9894(03)80155-1

Gaube, P., Chickadel, C., Branch, R., & Jessup, A. (2019). Satellite observations of sst-induced wind speed perturbation at the oceanic submesoscale. *Geophysical Research Letters*, *46*(5), 2690–2695. https://doi.org/10.1029/2018gl080807

Gévaudan, M., Jouanno, J., Durand, F., Morvan, G., Renault, L., & Samson, G. (2021). Influence of ocean salinity stratification on the tropical atlantic ocean surface. *Climate Dynamics*, *57*(1–2), 321–340. https://doi.org/10.1007/s00382-021-05713-z

Ghil, M., Allen, M., Dettinger, M., Ide, K., Kondrashov, D., Mann, M., et al. (2002). Advanced spectral methods for climatic time series. *Reviews of Geophysics*, *40*(1), 1–3. https://doi.org/10.1029/2000rg000092

Ghil, M., & Vautard, R. (1991). Interdecadal oscillations and the warming trend in global temperature time series. *Nature*, *350*(6316), 324–327. https://doi.org/10.1038/350324a0

Godfrey, J., & Lindstrom, E. (1989). The heat budget of the equatorial western pacific surface mixed layer. *Journal of Geophysical Research*, *94*(C6), 8007–8017. https://doi.org/10.1029/jc094ic06p08007

Groth, A., Feliks, Y., Kondrashov, D., & Ghil, M. (2017). Interannual variability in the north atlantic ocean's temperature field and its association with the wind stress forcing. *Journal of Climate*, *30*(7), 2655–2678. https://doi.org/10.1175/jcli-d-16-0370.1

Hall, K., Daley, A., Whitehall, S., Sandiford, S., & Gentemann, C. L. (2022). Validating salinity from smap and hycom data with saildrone data during eurec4a-oa/atomic. *Remote Sensing*, *14*(14), 3375. https://doi.org/10.3390/rs14143375

Hande, L., Siems, S. T., Manton, M. J., & Belusic, D. (2012). Observations of wind shear over the southern ocean. *Journal of Geophysical Research*, *117*(D12). https://doi.org/10.1029/2012jd017488

Hayes, S., McPhaden, M., & Wallace, J. (1989). The influence of sea-surface temperature on surface wind in the eastern equatorial pacific: Weekly to monthly variability. *Journal of Climate*, *2*(12), 1500–1506. https://doi.org/10.1175/1520-0442(1989)002<1500:tiosst>2.0.co;2

Hernandez, O., Jouanno, J., & Durand, F. (2016). Do the amazon and orinoco freshwater plumes really matter for hurricane-induced ocean surface cooling? *Journal of Geophysical Research: Oceans*, *121*(4), 2119–2141. https://doi.org/10.1002/2015jc011021

Hersbach, H., Bell, B., Berrisford, P., Hirahara, S., Horányi, A., Muñoz-Sabater, J., et al. (2020). The era5 global reanalysis [Dataset]. *Quarterly Journal of the Royal Meteorological Society*, *146*(730), 1999–2049. https://doi.org/10.1002/qj.3803

Jochumsen, K., Rhein, M., Hüttl-Kabus, S., & Böning, C. W. (2010). On the propagation and decay of north Brazil current rings. *Journal of Geophysical Research*, *115*(C10). https://doi.org/10.1029/2009jc006042

Johns, W. E., Lee, T. N., Schott, F. A., Zantopp, R. J., & Evans, R. H. (1990). The north Brazil current retroflection: Seasonal structure and eddy variability. *Journal of Geophysical Research*, *95*(C12), 22103–22120. https://doi.org/10.1029/jc095ic12p22103

Johns, W. E., Zantopp, R. J., & Goni, G. J. (2003). Cross-gyre transport by north Brazil current rings. *Interhemispheric Water Exchange in the Atlantic Ocean*. https://doi.org/10.1016/s0422-9894(03)80156-3

Karstensen, J., Lavik, G., Acquistapace, C., Baghen, G., Begler, C., & Bendinger, A. (2020). Eurec4a campaign, cruise no. msm89, 17. january-20. february 2020, bridgetown (Barbados)-bridgetown (Barbados), the ocean mesoscale component in the eurec4a++ field study.

Krishnamohan, K., Vialard, J., Lengaigne, M., Masson, S., Samson, G., Pous, S., et al. (2019). Is there an effect of bay of bengal salinity on the northern indian ocean climatological rainfall? Deep. *Sea Research Part II: Topical Studies in Oceanography*, *166*, 19–33. https://doi.org/10.1016/j.dsr2.2019.04.003

Kwiatkowski, L., & Orr, J. C. (2018). Diverging seasonal extremes for ocean acidification during the twenty-first century. *Nature Climate Change*, *8*(2), 141–145. https://doi.org/10.1038/s41558-017-0054-0

Lange, D., Behrendt, A., & Wulfmeyer, V. (2019). Compact operational tropospheric water vapor and temperature Raman lidar with turbulence resolution. *Geophysical Research Letters*, *46*(24), 14844–14853. https://doi.org/10.1029/2019gl085774

Laxenaire, R., Speich, S., Blanke, B., Chaigneau, A., Pegliasco, C., & Stegner, A. (2018). Anticyclonic eddies connecting the western boundaries of indian and atlantic oceans. *Journal of Geophysical Research: Oceans*, *123*(11), 7651–7677. https://doi.org/10.1029/2018jc014270

L'Hégaret, P., Schütte, F., Speich, S., Reverdin, G., Baranowski, D. B., & Czeschel, R. (2022). Ocean cross-validated observations from the r/vs l'atalante, maria s. merian and meteor and related platforms as part of the eurec 4 a-oa/atomic campaign. *Earth System Science Data Discussions*, 1–39.

Lindzen, R. S., & Nigam, S. (1987). On the role of sea surface temperature gradients in forcing low-level winds and convergence in the tropics. *Journal of the Atmospheric Sciences*, *44*(17), 2418–2436. https://doi.org/10.1175/1520-0469(1987)044<2418:otross>2.0.co;2

Liu, H., Li, W., Chen, S., Fang, R., & Li, Z. (2018). Atmospheric response to mesoscale ocean eddies over the south China sea. *Advances in Atmospheric Sciences*, *35*(9), 1189–1204. https://doi.org/10.1007/s00376-018-7175-x

Lloyd, S. (1982). Least squares quantization in pcm. *IEEE Transactions on Information Theory*, *28*(2), 129–137. https://doi.org/10.1109/tit.1982.1056489

Lukas, R., & Lindstrom, E. (1991). The mixed layer of the western equatorial pacific ocean. *Journal of Geophysical Research*, *96*(S01), 3343–3357. https://doi.org/10.1029/90jc01951

Ma, J., Xu, H., Dong, C., Lin, P., & Liu, Y. (2015). Atmospheric responses to oceanic eddies in the kuroshio extension region. *Journal of Geophysical Research: Atmospheres*, *120*(13), 6313–6330. https://doi.org/10.1002/2014jd022930

Ma, Z., Fei, J., Lin, Y., & Huang, X. (2020). Modulation of clouds and rainfall by tropical cyclone's cold wakes. *Geophysical Research Letters*, *47*(17), e2020GL088873. https://doi.org/10.1029/2020gl088873

Maes, C., & O'Kane, T. J. (2014). Seasonal variations of the upper ocean salinity stratification in the tropics. *Journal of Geophysical Research: Oceans*, *119*(3), 1706–1722. https://doi.org/10.1002/2013jc009366

Mahadevan, A., Jaeger, G. S., Freilich, M., Omand, M. M., Shroyer, E. L., & Sengupta, D. (2016). Freshwater in the bay of bengal: Its fate and role in air-sea heat exchange. *Oceanography*, *29*(2), 72–81. https://doi.org/10.5670/oceanog.2016.40

McDougall, T. J., Feistel, R., Millero, F. J., Jackett, D. R., Wright, D. G., King, B. A., et al. (2009). The international thermodynamic equation of seawater 2010 (TEOS-10): Calculation and use of thermodynamic properties. In *Global ship-based repeat hydrography manual, IOCCP* (Report 14).

Merchant, C. J., Embury, O., Roberts-Jones, J., Fiedler, E., Bulgin, C. E., Corlett, G. K., et al. (2014). Sea surface temperature datasets for climate applications from phase 1 of the european space agency climate change initiative (sst cci). *Geoscience Data Journal*, *1*(2), 179–191. https://doi.org/10.1002/gdj3.20

Meroni, A. N., Parodi, A., & Pasquero, C. (2018). Role of sst patterns on surface wind modulation of a heavy midlatitude precipitation event. *Journal of Geophysical Research: Atmospheres*, *123*(17), 9081–9096. https://doi.org/10.1029/2018jd028276

Mignot, J., Lazar, A., & Lacarra, M. (2012). On the formation of barrier layers and associated vertical temperature inversions: A focus on the northwestern tropical atlantic. *Journal of Geophysical Research*, *117*(C2). https://doi.org/10.1029/2011jc007435

Miller, J. R. (1976). The salinity effect in a mixed layer ocean model. *Journal of Physical Oceanography*, *6*(1), 29–35. https://doi.org/10.1175/1520-0485(1976)006<0029:tseiam>2.0.co;2

Minobe, S., Kuwano-Yoshida, A., Komori, N., Xie, S.-P., & Small, R. J. (2008). Influence of the gulf stream on the troposphere. *Nature*, *452*(7184), 206–209. https://doi.org/10.1038/nature06690

Mohr, W., Kinne, S., Baier, K., Baranowski, D., Chilinski, M., Gollop, J., et al. (2020). Eurec4a campaign, cruise no. m161, 17 jan 2020–3 mar 2020, bridgetown Barbados–ponta delgada Portugal.

Neggers, R., Stevens, B., & Neelin, J. D. (2006). A simple equilibrium model for shallow-cumulus-topped mixed layers. *Theoretical and Computational Fluid Dynamics*, *20*(5–6), 305–322. https://doi.org/10.1007/s00162-006-0030-1

Olivier, L., Boutin, J., Reverdin, G., Lefèvre, N., Landschützer, P., Speich, S., et al. (2022). Wintertime process study of the north Brazil current rings reveals the region as a larger sink for co 2 than expected. *Biogeosciences*, *19*(12), 2969–2988. https://doi.org/10.5194/bg-19-2969-2022

O'Neill, L. W., Chelton, D. B., Esbensen, S. K., & Wentz, F. J. (2005). High-resolution satellite measurements of the atmospheric boundary layer response to sst variations along the agulhas return current. *Journal of Climate*, *18*(14), 2706–2723. https://doi.org/10.1175/jcli3415.1

Pailler, K., Bourles, B., & Gouriou, Y. (1999). The barrier layer in the western tropical atlantic ocean. *Geophysical Research Letters*, *26*(14), 2069–2072. https://doi.org/10.1029/1999gl900492

Pasquero, C., Desbiolles, F., & Meroni, A. N. (2021). Air-sea interactions in the cold wakes of tropical cyclones. *Geophysical Research Letters*, *48*(2), e2020GL091185. https://doi.org/10.1029/2020gl091185

Pearson, G., Davies, F., & Collier, C. (2009). An analysis of the performance of the ufam pulsed Doppler lidar for observing the boundary layer. *Journal of Atmospheric and Oceanic Technology*, *26*(2), 240–250. https://doi.org/10.1175/2008jtecha1128.1

Peng, S., Yang, Q., Shupe, M. D., Xi, X., Han, B., Chen, D., et al. (2023). The characteristics of atmospheric boundary layer height over the arctic ocean during mosaic. *Atmospheric Chemistry and Physics*, *23*(15), 8683–8703. https://doi.org/10.5194/acp-23-8683-2023

Quinn, P. K., Thompson, E. J., Coffman, D. J., Baidar, S., Bariteau, L., Bates, T. S., et al. (2021). Measurements from the rv ronald h. brown and related platforms as part of the atlantic tradewind ocean-atmosphere mesoscale interaction campaign (atomic). *Earth System Science Data*, *13*(4), 1759–1790. https://doi.org/10.5194/essd-13-1759-2021

Renault, L., Masson, S., Oerder, V., Jullien, S., & Colas, F. (2019). Disentangling the mesoscale ocean-atmosphere interactions. *Journal of Geophysical Research: Oceans*, *124*(3), 2164–2178. https://doi.org/10.1029/2018jc014628

Renault, L., Molemaker, M. J., McWilliams, J. C., Shchepetkin, A. F., Lemarié, F., Chelton, D., et al. (2016). Modulation of wind work by oceanic current interaction with the atmosphere. *Journal of Physical Oceanography*, *46*(6), 1685–1704. https://doi.org/10.1175/jpo-d-15-0232.1

Reverdin, G., Olivier, L., Foltz, G., Speich, S., Karstensen, J., Horstmann, J., et al. (2021). Formation and evolution of a freshwater plume in the northwestern tropical atlantic in february 2020. *Journal of Geophysical Research: Oceans*, *126*(4), e2020JC016981. https://doi.org/10.1029/2020jc016981

Richardson, P., Hufford, G., Limeburner, R., & Brown, W. (1994). North Brazil current retroflection eddies. *Journal of Geophysical Research*, *99*(C3), 5081–5093. https://doi.org/10.1029/93jc03486

Roberts, J. B., Clayson, C. A., & Robertson, F. R. (2020). Seaflux data products v3 [Dataset]. *Down to Earth*. https://doi.org/10.5067/SEAFLUX/DATA101

Roberts, J. B., Clayson, C. A., Robertson, F. R., & Jackson, D. L. (2010). Predicting near-surface atmospheric variables from special sensor microwave/imager using neural networks with a first-guess approach. *Journal of Geophysical Research*, *115*(D19). https://doi.org/10.1029/2009jd013099

Seidel, D. J., Zhang, Y., Beljaars, A., Golaz, J.-C., Jacobson, A. R., & Medeiros, B. (2012). Climatology of the planetary boundary layer over the continental United States and europe. *Journal of Geophysical Research*, *117*(D17). https://doi.org/10.1029/2012jd018143

Shao, M., Ortiz-Suslow, D. G., Haus, B. K., Lund, B., Williams, N. J., Özgökmen, T. M., et al. (2019). The variability of winds and fluxes observed near submesoscale fronts. *Journal of Geophysical Research: Oceans*, *124*(11), 7756–7780. https://doi.org/10.1029/2019jc015236

Smith, W. H., & Sandwell, D. T. (1997). Global sea floor topography from satellite altimetry and ship depth soundings. Version 2. [Dataset]. *Science*, *277*(5334), 1956–1962. https://doi.org/10.1126/science.277.5334.1956

Speich, S. (2021). *The embarked science team: Eurec4a-oa. cruise report. 19 january–19 february 2020.* vessel: L'atalante. Ifremer.

Sprintall, J., & Tomczak, M. (1992). Evidence of the barrier layer in the surface layer of the tropics. *Journal of Geophysical Research*, *97*(C5), 7305–7316. https://doi.org/10.1029/92jc00407

Stephan, C. C., Schnitt, S., Schulz, H., Bellenger, H., De Szoeke, S. P., Acquistapace, C., et al. (2021). Ship-and island-based atmospheric soundings from the 2020 eurec¡ sup¿ 4¡/sup¿ a field campaign. *Earth System Science Data*, *13*(2), 491–514. https://doi.org/10.5194/essd-13-491-2021

Stevens, B., Bony, S., Farrell, D., Ament, F., Blyth, A., & Fairall, C. (2021). Others (2021). Eurec 4 a. *Earth System Science Data Discussions*, 1–78.

Subirade, C., L'Hégaret, P., Speich, S., Laxenaire, R., Karstensen, J., & Carton, X. (2023). Combining an eddy detection algorithm with in-situ measurements to study north Brazil current rings. *Remote Sensing*, *15*(7), 1897. https://doi.org/10.3390/rs15071897

Swart, S., du Plessis, M. D., Thompson, A. F., Biddle, L. C., Giddy, I., Linders, T., et al. (2020). Submesoscale fronts in the antarctic marginal ice zone and their response to wind forcing. *Geophysical Research Letters*, *47*(6), e2019GL086649. https://doi.org/10.1029/2019gl086649

Takatama, K., & Schneider, N. (2017). The role of back pressure in the atmospheric response to surface stress induced by the kuroshio. *Journal of the Atmospheric Sciences*, *74*(2), 597–615. https://doi.org/10.1175/jas-d-16-0149.1

Tanimoto, Y., Nakamura, H., Kagimoto, T., & Yamane, S. (2003). An active role of extratropical sea surface temperature anomalies in determining anomalous turbulent heat flux. *Journal of Geophysical Research*, *108*(C10). https://doi.org/10.1029/2002jc001750

Touzé-Peiffer, L., Vogel, R., & Rochetin, N. (2022). Cold pools observed during eurec 4 a: Detection and characterization from atmospheric soundings. *Journal of Applied Meteorology and Climatology*, *61*(5), 593–610. https://doi.org/10.1175/jamc-d-21-0048.1

Vautard, R., & Ghil, M. (1989). Singular spectrum analysis in nonlinear dynamics, with applications to paleoclimatic time series. *Physica D: Nonlinear Phenomena*, *35*(3), 395–424. https://doi.org/10.1016/0167-2789(89)90077-8

Vautard, R., Yiou, P., & Ghil, M. (1992). Singular-spectrum analysis: A toolkit for short, noisy chaotic signals. *Physica D: Nonlinear Phenomena*, *58*(1–4), 95–126. https://doi.org/10.1016/0167-2789(92)90103-t

Vialard, J., & Delecluse, P. (1998). An ogcm study for the toga decade. part i: Role of salinity in the physics of the western pacific fresh pool. *Journal of Physical Oceanography*, *28*(6), 1071–1088. https://doi.org/10.1175/1520-0485(1998)028<1071:aosftt>2.0.co;2

Villas Bôas, A., Sato, O., Chaigneau, A., & Castelão, G. (2015). The signature of mesoscale eddies on the air-sea turbulent heat fluxes in the south atlantic ocean. *Geophysical Research Letters*, *42*(6), 1856–1862. https://doi.org/10.1002/2015gl063105

Vogelezang, D., & Holtslag, A. (1996). Evaluation and model impacts of alternative boundary-layer height formulations. *Boundary-Layer Meteorology*, *81*(3–4), 245–269. https://doi.org/10.1007/bf02430331

Wallace, J. M., Mitchell, T., & Deser, C. (1989). The influence of sea-surface temperature on surface wind in the eastern equatorial pacific: Seasonal and interannual variability. *Journal of Climate*, *2*(12), 1492–1499. https://doi.org/10.1175/1520-0442(1989)002<1492:tiosst>2.0.co;2

Wang, Z., & Sassen, K. (2001). Cloud type and macrophysical property retrieval using multiple remote sensors. *Journal of Applied Meteorology and Climatology*, *40*(10), 1665–1682. https://doi.org/10.1175/1520-0450(2001)040<1665:ctampr>2.0.co;2

Weller, R., & Anderson, S. (1996). Surface meteorology and air-sea fluxes in the western equatorial pacific warm pool during the toga coupled ocean-atmosphere response experiment. *Journal of Climate*, *9*(8), 1959–1990. https://doi.org/10.1175/1520-0442(1996)009<1959:smaasf>2.0.co;2

Wick, G. A., Jackson, D. L., & Castro, S. L. (2023). Assessing the ability of satellite sea surface temperature analyses to resolve spatial variability–the northwest tropical atlantic atomic region. *Remote Sensing of Environment*, *284*, 113377. https://doi.org/10.1016/j.rse.2022.113377

Yang, H., Liu, J., Lohmann, G., Shi, X., Hu, Y., & Chen, X. (2016). Ocean-atmosphere dynamics changes associated with prominent ocean surface turbulent heat fluxes trends during 1958–2013. *Ocean Dynamics*, *66*(3), 353–365. https://doi.org/10.1007/s10236-016-0925-3

Zhang, D., Cronin, M. F., Meinig, C., Farrar, J. T., Jenkins, R., Peacock, D., et al. (2019). Comparing air-sea flux measurements from a new unmanned surface vehicle and proven platforms during the spurs-2 field campaign. *Oceanography*, *32*(2), 122–133. https://doi.org/10.5670/oceanog.2019.220

Zheng, Y. (2019). Theoretical understanding of the linear relationship between convective updrafts and cloud-base height for shallow cumulus clouds. part i: Maritime conditions. *Journal of the Atmospheric Sciences*, *76*(8), 2539–2558. https://doi.org/10.1175/jas-d-18-0323.1